Electronic Supplementary Information

Oxygen Surface Exchange Kinetics and Stability of $(La,Sr)_2CoO_{4\pm\delta}/La_{1-x}Sr_xMO_{3-\delta}$ (M = Co and Fe) Hetero-interfaces at Intermediate Temperatures

Dongkyu Lee[1,2,+], Yueh-Lin Lee[1,2,+], Wesley T. Hong[1,3], Michael D. Biegalski[4], Dane Morgan[5,*], and Yang Shao-Horn[1,2,3,*]

[1]Electrochemical Energy Laboratory, [2]Department of Mechanical Engineering, and [3]Department of Materials Science and Engineering, Massachusetts Institute of Technology, 77 Massachusetts Avenue, Cambridge, Massachusetts 02139, United States

[4]Center for Nanophase Materials Sciences, Oak Ridge National Laboratory, Oak Ridge, Tennessee 37831, United States

[5]Department of Materials Science and Engineering, University of Wisconsin–Madison, Madison, Wisconsin 53706, USA

Index	**Page**

Experimental Details

Target Synthesis. Both $La_{0.6}Sr_{0.4}Co_{0.2}Fe_{0.8}O_{3-\delta}$ ($LSCF_{113}$) and $LaSrCoO_{4\pm\delta}$ (LSC_{214}) were prepared by the Pechini methods. $La(NO_3)_3 \bullet 6H_2O$, $Co(NO_3)_3 \bullet 6H_2O$, $Fe(NO_3)_3 \bullet 9H_2O$, $Sr(NO_3)_2$, and separately $La(NO_3)_3 \bullet 6H_2O$, $Co(NO_3)_3 \bullet 6H_2O$, $Sr(NO_3)_2$ were dissolved in de-ionized water with ethylene glycol, and citric acid (Sigma-Aldrich, USA) mixture to synthesize $LSCF_{113}$ and LSC_{214} respectively. After esterification at 100 ºC, the resin was charred at 400 ºC and finally calcined at 1000 ºC in air for 12 hours. The $La_{0.8}Sr_{0.2}CoO_{3-\delta}$ (LSC_{113}) and $Gd_{0.2}Ce_{0.8}O_2$ (GDC) were also prepared by the Pechini methods[1]. $La(NO_3)_3 \bullet 6H_2O$, $Sr(NO_3)_2$, $Mn(NO_3)_2 \bullet 6H_2O$, and separately $Gd(NO_3)_3$ and $Ce(NO_3)_3$ were dissolved in de-ionized water with ethylene glycol, and citric acid (Sigma-Aldrich, USA) mixture to synthesize LSM82 and GDC respectively. After esterification at 100 ºC, the resin was charred at 400 ºC and finally calcined at 1000 ºC in air for 12 hours. Pulsed laser deposition (PLD) target pellets with 25 mm diameter were subsequently fabricated by uniaxial pressing at 50 MPa. The $LSCF_{113}$, LSC_{113}, LSC_{214}, and GDC pellets were fully sintered at 1,300 ºC in air for 6 hours, 1,200 ºC in air for 10 hours, 1,350 ºC in air for 12 hours, and 1,100 ºC in air for 14 hours, respectively.

Sample preparation. Single crystal 9.5 mol% Y_2O_3-stabilized ZrO_2 (YSZ) wafers with (001) orientation and dimensions of 10 × 5 × 0.5 mm (MTI corporation, USA), were used as substrate. Prior to LSC_{214}, $LSCF_{113}$, LSC_{113}, and GDC deposition, platinum ink (Pt) (#6082, BASF, USA) counter electrodes were painted on one side of the YSZ and dried at 900 ºC in air for 1 hour. PLD was performed using a KrF excimer laser at λ= 248 nm, 10 Hz pulse rate and 45 mJ pulse energy under $p(O_2)$ of 50mTorr with 500 pulses of GDC (~5 nm) at 550 °C, followed by 15,000 pulses of $LSCF_{113}$ (~63 nm) at 650 ºC. PLD was also performed using the same laser conditions

under $p(O_2)$ of 100mTorr with 500 pulses of GDC (~5 nm) at 550 °C, followed by 15,000 pulses of LSC_{113} (~85 nm) at 650 ºC. The film thicknesses were determined by atomic force microscopy (AFM). The utilization of reflection high-energy electron diffraction (RHEED) enabled diagnostic *in-situ* monitoring of the LSC82 film growth. Immediately after completing the $LSCF_{113}$ base film deposition, LSC_{214} films were subsequently deposited; for the LSC_{214} surface coverages consisting of 50 pulses (~0.3 nm), 150 pulses (~0.8 nm), 500 pulses (~2.6 nm), and 1,000 pulses (~5 nm). The LSC_{214} films (~2.6 nm) were also subsequently deposited on the LSC_{113} base film. LSC_{214} decoration layer thickness is extrapolated from AFM of the 500 pulses and 1,000 pulses LSC_{214} coverage on $LSCF_{113}$. After completing the final deposition, the sample was cooled to room temperature in the PLD chamber for ~1 hour under an oxygen partial pressure of 50 mTorr.

HRXRD analysis of LSC_{214} decorated LSC_{113} thin film. Normal XRD data (Fig. S2a †) of the undecorated LSC_{113} and LSC_{214}-decorated LSC_{113} films clearly show the presence of the $(00l)_{pc}$ (l is integer) peaks of LSC_{113} and $(00l)_{cubic}$ (l is even) peaks of GDC and YSZ, indicating that the LSC_{113} film grew epitaxially with the following epitaxial relationships: $(001)_{pc}LSC_{113}$ // $(001)_{cubic}GDC$ // $(001)_{cubic}YSZ$. With LSC_{214} coverage equal to ~2.6 nm in thickness, the $(00l)_{tetra.}$ (l is integer) peaks of LSC_{214} was found to show, representing $(001)_{tetra.}LSC_{214}$ // $(001)_{pc}LSC_{113}$ // $(001)_{cubic}GDC$ // $(001)_{cubic}YSZ$. The subscript "tetra." denotes the tetragonal notation. Off-normal phi-scan analysis of the undecorated LSC_{113} and LSC_{214}-decorated LSC_{113} films shows that LSC_{214} $\{103\}_{tetra.}$, LSC_{113} $\{101\}_{pc}$, GDC $\{202\}_{cubic}$ and YSZ $\{202\}_{cubic}$ have strong peaks with 4-fold cubic symmetry (Fig. S2b†), which reveals the in-plane crystallographic relationships between GDC and YSZ (a cube-on-cube alignment), LSC_{113} and GDC (an in-plane 45º rotation

with $[100]_{pc}LSC_{113}$ // $[110]_{cubic}GDC$ // $[110]_{cubic}YSZ$), and LSC_{113} and LSC_{214} (no rotation with $[100]_{pc}LSC_{113}$ // $[100]_{tetra.}LSC_{214}$), as shown in Fig. S2c†.

Relaxed lattice parameter determination by HRXRD. The Relaxed lattice parameter $\hat{a}$ and $\hat{c}$ are derived from the following equation (where $\hat{a}$ and $\hat{c}$ are the relaxed lattice parameters for the film in an unstrained state),[2-4] $\frac{(c-\hat{c})}{\hat{c}} = \frac{-2\nu(a-\hat{a})}{1-\nu \quad \hat{a}}$, assuming $\hat{a} = \hat{c}$, and ν = 0.25.[2] The in-plane strain is given by: $\varepsilon_{aa} = \frac{(a-\hat{a})}{\hat{a}}$ and the out of plane strain by: $\varepsilon_{cc} = \frac{(c-\hat{c})}{\hat{c}}$

Microelectrodes Fabrication. *In situ* electrochemical impedance spectroscopy (EIS) measurements were conducted to probe ORR activity on geometrically well-defined LSC_{214}-decorated $LSCF_{113}$ microelectrodes fabricated by photolithography and acid etching, where sintered porous Pt sintered onto the backside of the YSZ substrate served as the counter electrode. OCG positive photoresist (Arch Chemical Co., USA) was applied on the LSC_{214}-decorated $LSCF_{113}$ surface and patterned using a mask aligner (Karl Süss, Germany, λ = 365 nm). The photoresist was developed using Developer 934 1:1 (Arch Chemical Co., USA) and the thin films were etched in hydrochloric acid (HCl) to remove LSC_{214}-decorated $LSCF_{113}$ film excess and create the circular microelectrodes (diameters ~50 μm, ~100 μm, ~150 μm, and ~200 μm, exact diameter determined by optical microscopy). The LSC_{214}-decorated LSC_{113} microelectrodes were also fabricated by using the same manner. Before electrochemical testing, microelectrode geometry and morphology was examined by optical microscopy (Carl Zeiss, Germany) and atomic force microscopy (AFM) (Veeco, USA).

Electrochemical Characterization. Fig. S4b† and S4c† detail the equivalent circuit and corresponding Nyquist plot for this experimental system. *ZView* software (Scribner Associates, USA) was used to construct the equivalent circuit and perform complex least squares fitting. The EIS data were fitted using a standard resistor (R_1) for *HF* and resistors (R_2) in parallel with a constant phase elements (CPE_2) for *MF* and *LF* (R_1-(R_2/CPE_2)-(R_{ORR}/CPE_{ORR})). Based on the $p(O_2)$ dependence of the three features, physical or chemical process with regard to each frequency range can be determined.[5-8] The *HF* feature was found unchanged with $p(O_2)$, and its magnitude and activation energy (~1.15 eV) were comparable to those of oxygen ion conduction in YSZ reported previously[9]. The *MF* feature, which was found to have a $p(O_2)$ independent feature, was attributed to interfacial transport of oxygen ions between the $LSCF_{113}$ film and the GDC layer. In addition, the magnitude of its capacitance was relatively small (~10^{-6} F) compared to the *LF* feature (~10^{-3} F). The *LF* feature was found to have a strong $p(O_2)$ dependence. The resistance of the *LF* feature drastically increases as oxygen partial pressure decreases. In the case of thin film samples, the magnitude of capacitance is due to the oxygen content change in the films. Therefore, the electrode oxygen surface reaction corresponds with the *LF* feature. We obtained values for R_{ORR} and knowing the area of the microelectrode ($A_{electrode} = 0.25\ \pi\ d_{electrode}^2$). Then, we can determine the ORR area specific resistance ($ASR_{ORR} = R_{ORR} \cdot A_{electrode}$). The electrical surface exchange coefficient (k^q), which is comparable to k^*,[10] was determined using the expression,[11, 12]

$$k^q = RT / 4F^2 R_{ORR} A_{electrode} c_o \quad (1)$$

where R is the universal gas constant (8.314 J mol^{-1} K^{-1}), T is the absolute temperature, F is the Faraday's constant (96,500 C mol^{-1}), and c_o is the lattice oxygen concentration in $LSCF_{113}$ where

$$c_o = (3-\delta)/V_m, \quad (2)$$

V_m is the molar volume of $LSCF_{113}$ at room temperature. In this study, c_o was calculated with δ extracted from previous reported values.[13]

The electrical surface exchange coefficient (k^q) of the LSC_{113} and LSC_{214}-decorated LSC_{113} thin film was also determined using the same manner. EIS data collected from the LSC_{214}-decorated LSC_{113} film at 550 °C as a function of $p(O_2)$ are shown in Fig. S5†. The predominant semicircle was found to increase with decreasing oxygen partial pressure, where EIS data of the LSC_{214}-decorated LSC_{113} was found to show nearly perfect semicircle impedances.[5] Considering the fact that the film thickness is smaller than the critical thickness (~1 nm for bulk LSC_{113} at 550 °C[14, 15]), the $p(O_2)$-dependent impedance responses suggest that the oxygen surface exchange kinetics governs the oxygen electrocatalysis on the film surface.

The LSC_{214} surface coverage may change the c_o value of the system. For estimating this influence we compared LSC_{214} c_o values with $LSCF_{113}$ c_o values. However, calculated c_o values for LSC_{214} were only ~1 - 2 % different from those for $LSCF_{113}$. We therefore decide to use c_o values for $LSCF_{113}$ for all samples. Similarly, calculated c_o values for LSC_{214} were only ~1 - 2 % different from those for LSC_{113}.

VSC, indicative of changes in the oxygen nonstoichiometry induced by changes in the electrical potential, can be obtained from EIS data via the expression[16]

$$VSC = [1/(A_{electrode} \bullet \text{thickness})]((R_{ORR})^{1-n}Q)^{1/n}, \quad (3)$$

where Q is the non-ideal "capacitance", and n is the non-ideality factor of *CPE*. The fitted values of n for semi-circle CPE_{ORR} were found to range from ~ 0.96 to 1.0 over the entire pO_2 range examined (n =1, ideal).

Experimental details of auger electron spectroscopy (AES). In AES, the obtained energy spectrum for a particular element is always situated on a large background (low signal-to-noise ratio), which arises from the vast number of so-called secondary electrons generated by a multitude of inelastic scattering processes. To obtain better sensitivity for detection of the elemental peak positions, the AES spectra from this study are presented in the differentiated form. Elemental quantification of AES spectra utilized relative sensitivity factors (RSFs) of 0.059, 0.027, 0.076, 0.178, and 0.212 for La_{MNN}, Sr_{LMM}, Co_{LMM}, Fe_{LMM}, and O_{KLL}, respectively, as supplied by the AES manufacturer (Physical Electronics). In addition, the Inelastic-Mean-Free-Path (IMFP) was calculated to correct signal intensity for their different IMFPs (information depth). IMFPs were calculated using the NIST Standard Reference Database 71 "NIST Electron Inelastic- Mean-Free-Path Database" version 1.2. The software program provides the ability to predict the IMFP for inorganic compounds supplying the stoichiometric composition of La (0.6), Sr (0.4), Co (0.2), Fe (0.8), and O (3), the number of valence electrons per molecule (assumed to be 24.8), the density (6.36 g/cm^3) and a band gap energy (for which we are assuming 0 eV as $LSCF_{113}$ is metallic like at high temperatures; additionally when assuming a band gap of an insulator 5 eV, the IMFP increases by ~0.03 nm). The IMFP for La, Sr, Co and Fe were determined to be 1.395, 2.667, 1.607, and 1.404 nm, respectively. A relative depth-scaling factor (σ_i) was determined as:

$$\sigma_i = \int_0^{\lambda_i \infty} \frac{1}{\lambda_i} \exp\left(-\frac{x}{\lambda_i}\right) dx \,, \qquad (4)$$

where λ_i is the IMFP, yielding $\sigma_{Sr} = 0.41$, $\sigma_{Co} = 0.58$, and σ_{La} and $\sigma_{Fe} = 0.63$. The intensities from different elements were scaled using $I_{scaled} = I_{measured} \bullet \sigma_{Si}/S_i$. Similarly, the IMFP for La, Sr, and Co of LSC_{113} was determined to be 1.1.337, 2.549, and 1.337 nm, respectively, by using the the stoichiometric composition of La (0.8), Sr (0.2), Co (1), and O (3), the number of valence

electrons per molecule (assumed to be 29.8), the density (6.931 g/cm^3) and a band gap energy (assumed 0 eV). The obtained values of the relative depth-scaling factor for LSC_{113} are thus approximately equal to those of $LSCF_{113}$. The La and Sr concentration (c_{La} or c_{Sr}) was obtained by normalizing to the their sum, $c_i=I_i/(I_{La}+I_{Sr})$. The Co concentration was also obtained by using the same manner.

Details of Density Functional Theory (DFT) Calculations and *Ab Initio* Thermodynamic Analysis

Density functional theory calculations

Spin polarized Density Functional Theory (DFT) calculations were preformed with the Vienna *Ab-initio* Simulation Package[17, 18] using the Projector-Augmented plane-Wave method[19] with a cutoff of 450 eV. Exchange-correlation was treated in the Perdew-Wang-91[20] Generalized Gradient Approximation (GGA). The pseudopotential configurations for each atom are as follows: La: $5s^2 5p^6 5d^1 6s^2$, Sr_sv: $4s^2 4p^6 5s^2$, Fe_pv: $3p^6 3d^7 4s^1$, Co: $3d^8 4s^1$ and O_s: $2s^2 2p^4$. The GGA+*U* calculations[21] are performed with the simplified spherically averaged approach,[22] where the U_{eff} (U_{eff} = Coulomb *U* - exchange *J*) is applied to *d* electrons. (U_{eff}(Fe) = 4.0 eV and U_{eff}(Co) = 3.3 eV)[23, 24]. All calculations are performed in the ferromagnetic state in order to use a consistent and tractable set of magnetic structures, and the spin states for the calculated $La_{0.8}Sr_{0.2}CoO_{3-\delta}$ (LSC_{113}), $(La_{0.5}Sr_{0.5})_2CoO_4$ (LSC_{214}), and $La_{0.6}Sr_{0.4}Fe_{0.8}Co_{0.2}O_{3\pm\delta}$ ($LSCF_{113}$) systems are: Fe: high spin and Co: intermediate/high spin. While elevated temperatures used during synthesis and electrochemical testing in this study is expected to be in a paramagnetic state, such disordered moments are significantly more difficult to model and we believe that the trends and conclusions identified here would not be altered by using random spin arrangements.

Bulk Sr_{La} substitution energy calculations

Calculations for Sr_{La} substitution energies in bulk $LSCF_{113}$ and LSC_{113} are simulated using a $2a_{pv}\times2a_{pv}\times2a_{pv}$ pseudocubic supercell structure of $La_{0.625}Sr_{0.375}Fe_{0.75}Co_{0.25}O_{3\pm\delta}$ (a_{pv}($LSCF_{113}$) = 3.91 Å, where a_{pv} is the GGA+U perovskite lattice constant) and $La_{0.75}Sr_{0.25}CoO_3$ (with $a_{pv}(La_{0.75}Sr_{0.25}CoO_3)$ = 3.88 Å) with 2×2×2 k-point mesh and 450 eV plane-wave energy cut-off.

Sr_{La} substitution energy in bulk $(La_{0.5}Sr_{0.5})_2CoO_{4\pm\delta}$ is simulated using a $2a_{rp}\times2a_{rp}\times c_{rp}$ supercell structure of $(La_{0.5}Sr_{0.5})_2CoO_4$ with the lattice constants $a_{rp}(LSC_{214})$ = 3.86 Å, $c_{rp}(LSC_{214})$ = 12.50 Å. The bulk $LSCF_{113}$ supercell configurations are illustrated in Fig. S8a† and S8b†. The Sr_{La} substitution energy for $La_{0.625}Sr_{0.375}Fe_{0.75}Co_{0.25}O_3$ ($La_{0.75}Sr_{0.25}CoO_3$) bulk was taken as the difference in energies between a $La_{0.5}Sr_{0.5}Fe_{0.75}Co_{0.25}O_3$ ($La_{0.625}Sr_{0.375}CoO_3$) bulk and a $La_{0.625}Sr_{0.375}Fe_{0.75}Co_{0.25}O_3$ ($La_{0.625}Sr_{0.375}CoO_3$) bulk. Similarly, the Sr_{La} substitution energy for $(La_{0.5}Sr_{0.5})_2CoO_{4\pm\delta}$ was calculated using the total energy difference between (($La_{0.5}Sr_{0.5})_2CoO_4$) and ($La_{0.4375}Sr_{0.5625})_2CoO_4$). The supercell configurations are illustrated in Fig S8c†.

$LSCF_{113}$-LSC_{214} interface Sr_{La} substitution energy calculations

The LSC_{214}-$LSCF_{113}$ heterointerface was simulated with a fully periodic 176-atom supercell ($2a_{113}\times2a_{113}$ supercell in the x-y plane ($a_{113} = a_{pv}^{DFT}(LSCF_{113})$ =3.91 Å) with 12-layers of $La_{0.625}Sr_{0.375}Fe_{0.75}Co_{0.25}O_3$ and 6-layers of $(La_{0.5}Sr_{0.5})_2CoO_4$ along z where c_{214}=12.42 Å), similar to the previous LSC_{214}-LSC_{113} heterointerface structural model. The cation arrangements for $LSCF_{113}$ are illustrated in Fig. S9†.

***Ab initio* LSC_{113} and $LSCF_{113}$ (001) surface stability analysis**

In this section, we discuss on the *ab intio* thermodynamic analysis approach[25, 26] performed in this work for modeling LSC_{113} and $LSCF_{113}$ (001) AO and BO_2 surface stability at a given $p(O_2)$ and temperature under SOFC conditions. In the analysis, empirical O_2 gas phase thermodynamic data[27] is utilized for the temperature dependence of the O_2 gas free energy.[28] In addition, approximations are made in free energies of solid phases by neglecting electronic, magnetic, and other contributions except for vibration. The vibrational contribution is treated for oxygen in

solid phases based on the Einstein model with the mean field harmonic oscillator approximation for all the relevant oxides included in this work, as will be described below. These neglected free energies contributions are expected to be within the inherent energetic error (which we estimate at ±0.2 eV per formula unit based on formation energy comparisons to experiments[29] and in this work in Table S1†) of our DFT+U modeling approach. Anther approximation made here is to assume $\mu_M^{s,vib}(T)$ is equal in all the solid oxide phases, based on the Neumann-Kopp rule,[30] which leads to cancelation of $\mu_M^{s,vib}(T)$ between products and reactants of chemical reactions in which metal constituents are remained in the solid oxide phases.

a. Effective chemical potential of oxygen

The chemical potential of oxygen at a given T and oxygen partial pressure P is defined as follows[24, 28, 31] for the *ab initio* thermodynamic analysis:

$$\mu_{O_2}^{gas}(T,P)=\frac{1}{2}\begin{bmatrix} E_{DFT}(O_2^{gas}) \\ +\left(h_{O_2}^{gas}(T,P^0)-h_{O_2}^{gas}(T^0,P^0)\right)-T\cdot s_{O_2}^{gas}(T,P^0) \\ +k\cdot T\cdot \ln(\frac{P}{P^0}) \\ +\delta h_{O_2}^0 \end{bmatrix} \quad (5)$$

where $E_{DFT}(O_2^{gas})$ is the calculated DFT total energy of an O_2 molecule at T = 0 K, $h_{O_2}^{gas}(T,P^0)$ and $h_{O_2}^{gas}(T^0,P^0)$ are the O_2 gas enthalpy at the specified T and the standard temperature T^0 = 25 ºC under the oxygen partial pressure $P^0 = 1$ atm, $s_{O_2}^{gas}(T,P^0)$ is the O_2 gas entropy at the

specified T under the oxygen partial pressure P^0 = 1 atm (both the $\left(h_{O_2}^{gas}(T,P^0)-h_{O_2}^{gas}(T^0,P^0)\right)$and $s_{O_2}^{gas}(T,P^0)$ terms can be obtained from the NIST Thermodynamic database[27]), k is the Boltzmann constant, P is the specified oxygen partial pressure, and $\delta h_{O_2}^0$ is the DFT O_2 energy correction for error of the oxygen energy in the gas phase O_2 molecule vs. in a solid, fit with the experimental oxide formation enthalpies at the standard condition[24, 32].

To account for the fact that the thermodynamic quantities of the O_2 gas phase are taken from the empirical data, which contains kinetic energy (translation, rotation, and vibration) contributions (other contributions such as electronic energy are assumed to be small and can be neglected), while the total energy of the oxide solid phase calculated from DFT does not contain the vibrational contribution, it is convenient to define an effective oxygen chemical potential, $\mu_O^{eff}(T,P)$:

$$\begin{aligned}\mu_O^{eff}(T,P) &= \mu_O^{gas}(T,P)-\mu_O^{s,vib}(T)\\ &= \mu_O^{gas}(T,P)-(\bar{G}_O^{s,vib}(T)-\bar{H}_O^{s,vib}(T_0))\end{aligned} \quad (6)$$

where $\mu_O^{s,vib}(T)$ is the vibrational contribution to the oxygen chemical potential in the solid oxides, and $\bar{G}_O^{s,vib}(T)$ and $\bar{H}_O^{s,vib}(T_0)$ are the vibrational portions of the partial molar Gibbs free energy at temperature T and enthalpy at T = 25 ºC for O in the solid. The oxygen vibrational contribution to the solid oxide phase is approximated with a simple Einstein model with the Einstein temperature θ_E = 500 K[24].

$$\bar{G}_O^{s,vib}(T) = k \cdot T \cdot (\sum_j \ln\left[2 \cdot \sinh\left(\frac{\theta_E}{2T}\right)\right] = 3 \cdot k \cdot T \cdot \ln\left[2 \cdot \sinh\left(\frac{\theta_E}{2T_0}\right)\right] \quad (7)$$

$$\bar{H}_O^{s,vib}(T_0) = k \cdot T \cdot (\sum_j \frac{\theta_E}{2T_0} \ln\left[2 \cdot \coth\left(\frac{\theta_E}{2T_0}\right)\right] = 3 \cdot k \cdot T \cdot \frac{\theta_E}{2T_0} \cdot \ln\left[2 \cdot \coth\left(\frac{\theta_E}{2T_0}\right)\right] \quad (8)$$

where j=3 is for the vibrational degrees of freedom of oxygen ion in the solid. We note that the subtraction of $\bar{H}_O^{s,vib}(T_0)$ is necessary as this term is already accounted for in $\delta h_{O_2}^0$ of Equation (5). In addition, changing θ_E = 500 K by 50% in either direction from 250 to 750 K does not qualitatively impact any of our conclusions so no effort at a more quantitative model was attempted[31].

By using the effective oxygen chemical potential described above, the calculated DFT energies of the solid phases can be incorporated to include the temperature T and oxygen partial pressure P dependences for chemical reactions involving exchange of oxygens between the O_2 gas phase and solid oxide phases with a mean-field type vibrational parameter (i.e., Einstein temperature θ_E) for oxygen in the solid oxides.

To assess the energetic accuracy of the *ab initio* thermodynamic method described above, we compare the calculated *ab initio* oxide formation energies (reaction energies of forming the perovskite and the Ruddlesden Popper phases from binary oxides and oxygen gas phase) at room temperature vs. the reported experimental oxide formation enthalpies in the literature,[33-35] as shown in Table S1†. It is seen that the differences between the theoretical and experimental

results are within the estimated error range of ±0.2 eV per formula unit for the relevant perovskite and Ruddlesden Popper compounds in this work.

b. Effective chemical potentials of metals in binary oxides

The Gibbs free energy per formula unit of binary metal oxides can be written as follows:

$$g(MO_y) = \mu_M^{solid} + y \cdot \mu_O^{solid} \tag{9}$$

where μ_M^{solid} is the chemical potential of a metal constituent M in solid binary oxides. For equilibrium between the binary oxide phases and the O_2 gas phase at a given T and P, the chemical potential of oxygen is the same in the solid oxide phase and the O_2 gas phase: $\mu_O^{gas}(T,P) = \mu_O^{solid}$. Therefore, the chemical potentials of metals, μ_M^{solid}, can be written as:

$$\mu_M^{solid} = g(MO_y) - y \cdot \mu_O^{gas}(T,P) \tag{10}$$

By splitting the free energy $g(MO_y)$ into the calculated DFT total energy, $E^{DFT}(MO_y)$, and the vibrational contributions of metals ($\mu_M^{s,vib}(T)$) and oxygen ($\mu_O^{s,vib}(T)$) in the MO_y oxide, Equation (10) becomes:

$$\begin{aligned}
\mu_M^{solid} &= g(MO_y) - y \cdot \mu_O^{gas}(T,P) \\
&= \left[E^{DFT}(MO_y) + \mu_M^{s,vib}(T) + \mu_O^{s,vib}(T) \right] - y \cdot \mu_O^{gas}(T,P) \\
&= \left[E^{DFT}(MO_y) + \mu_M^{s,vib}(T) \right] - y \cdot \left[\mu_O^{gas}(T,P) - \mu_O^{s,vib}(T) \right] \\
&= \left[E^{DFT}(MO_y) + \mu_M^{s,vib}(T) \right] - y \cdot \mu_O^{eff}(T,P)
\end{aligned} \tag{11}$$

where $\mu_O^{eff}(T,P)$ is the effective oxygen chemical potential defined in Equation (6). For example, the chemical potentials of La, Sr, Co, and Fe in the binary oxides form of La_2O_3, SrO, Co_3O_4, and Fe_2O_3 at a given T and P can be expressed as follows:

$$\mu_{La}\left(La_2O_3\right)=\frac{1}{2}\left(E^{DFT}(La_2O_3)-3\cdot\mu_O^{eff}(T,P)\right)+\mu_{La}^{s,vib}\left(T\right) \quad (12)$$

$$\mu_{Sr}\left(SrO\right)=E^{DFT}(SrO)-\mu_O^{eff}(T,P)+\mu_{Sr}^{s,vib}\left(T\right) \quad (13)$$

$$\mu_{Co}\left(Co_3O_4\right)=\frac{1}{3}\left(E^{DFT}(Co_3O_4)-4\cdot\mu_O^{eff}(T,P)\right)+\mu_{Co}^{s,vib}\left(T\right) \quad (14)$$

$$\mu_{Fe}(Fe_2O_3)=\frac{1}{2}(E^{DFT}(Fe_2O_3)-3\cdot\mu_O^{eff}(T,P))+\mu_{Fe}^{s,vib}(T) \quad (15)$$

where $E^{DFT}(La_2O_3)$, $E^{DFT}(SrO)$, $E^{DFT}(Co_3O_4)$, and $E^{DFT}(Fe_2O_3)$ are the calculated *ab initio* total energies of La_2O_3, SrO, Co_3O_4, and Fe_2O_3 normalized as per formula unit.

Due to the assumption made previously to set $\mu_M^{s,vib}(T)$ equal in the different solid oxide phases, it is convenient to define effective chemical potential quantities for the metal constituents for Equations (12)~(15), by moving the $\mu_M^{s,vib}(T)$ from the right hand side to the left hand side of the equation:

$$\mu_{La}^{eff}\left(La_2O_3\right)\equiv\mu_{La}\left(La_2O_3\right)-\mu_{La}^{s,vib}\left(T\right)=\frac{1}{2}\left(E^{DFT}(La_2O_3)-3\cdot\mu_O^{eff}(T,P)\right) \quad (12')$$

$$\mu_{Sr}^{eff}\left(SrO\right)\equiv\mu_{Sr}\left(SrO\right)-\mu_{Sr}^{s,vib}\left(T\right)=E^{DFT}(SrO)-\mu_O^{eff}(T,P) \quad (13')$$

$$\mu_{Co}^{eff}(Co_3O_4) \equiv \mu_{Co}(Co_3O_4) - \mu_{Co}^{s,vib}(T) = \frac{1}{3}\left(E^{DFT}(Co_3O_4) - 4\cdot\mu_O^{eff}(T,P)\right) \quad (14')$$

$$\mu_{Fe}^{eff}(Fe_2O_3) \equiv \mu_{Fe}(Fe_2O_3) - \mu_{Fe}^{s,vib}(T) = \frac{1}{2}\left(E^{DFT}(Fe_2O_3) - 3\cdot\mu_O^{eff}(T,P)\right) \quad (15')$$

The effective chemical potential quantities for the metals in binary oxides will be further used as boundary conditions for perovskites in the construction of the bulk perovskite phase diagram.

c. Effective chemical potentials of metals in perovskites

For the $La_{1-x}Sr_xCo_yFe_{1-y}O_3$ perovskite phase, the Gibbs free energy per formula unit of $La_{1-x}Sr_xCo_yFe_{1-y}O_3$ can be written as follows:

$$g(La_{1-x}Sr_xCo_yFe_{1-y}O_3) = [(1-x)\cdot\mu_{La}^{PV} + x\cdot\mu_{Sr}^{PV}] + [(y\cdot\mu_{Co}^{PV} + (1-y)\cdot\mu_{Fe}^{PV}] + 3\mu_O^{PV}(T) \quad (16)$$

where PV denotes the perovskite phase. Again, here we split the metal chemical potentials of $La_{1-x}Sr_xCo_yFe_{1-y}O_3$ into the internal energy (E_{La}^{PV}, E_{Sr}^{PV}, E_{Co}^{PV}, and E_{Fe}^{PV}), and vibrational contributions of metals $\mu_M^{s,vib}(T)$, as well as the configurational entropy term $k\cdot T[x\cdot\ln(x) + (1-x)\cdot\ln(1-x)]$ for the A site and $k\cdot T[y\cdot\ln(y) + (1-y)\cdot\ln(1-y)]$ for the B site. Similarly, the oxygen chemical potential ($\mu_O^{PV}(T)$) in the perovskite can be split into the internal energy (E_O^{PV}), and the vibrational contribution $\mu_O^{s,vib}(T)$. The configurational entropy term for the oxygen lattice sites is zero when the O sites are fully occupied in the perovskite phase. Therefore,

$$g(La_{1-x}Sr_xCo_yFe_{1-y}O_3)$$

$$= \left\{ \begin{array}{l} [(1-x)\cdot E_{La}^{PV} + x\cdot E_{Sr}^{PV}] + [(y\cdot E_{Co}^{PV} + (1-y)\cdot E_{Fe}^{PV}] + 3\cdot E_{O}^{PV} \\ +k\cdot T[x\cdot \ln(x) + (1-x)\cdot \ln(1-x)] \\ +k\cdot T[y\cdot \ln(y) + (1-y)\cdot \ln(1-y)] \\ +[(1-x)\cdot \mu_{La}^{s,vib}(T) + x\cdot \mu_{Sr}^{s,vib}(T)] + [(y\cdot \mu_{Co}^{s,vib}(T) + (1-y)\cdot \mu_{Fe}^{s,vib}(T)] + 3\cdot \mu_{O}^{s,vib}(T) \end{array} \right\} \quad (17)$$

Here, the sum of the internal energy terms (E_{La}^{PV}, E_{Sr}^{PV}, E_{Co}^{PV}, E_{Fe}^{PV}, and E_{O}^{PV}) can be replaced by the calculated total energy of perovskite from DFT, i.e. $E^{DFT}(La_{1-x}Sr_xCo_yFe_{1-y}O_3)$:

$$g(La_{1-x}Sr_xCo_yFe_{1-y}O_3)$$

$$= \left\{ \begin{array}{l} E^{DFT}(La_{1-x}Sr_xCo_yFe_{1-y}O_3) \\ +k\cdot T[x\cdot \ln(x) + (1-x)\cdot \ln(1-x)] \\ +k\cdot T[y\cdot \ln(y) + (1-y)\cdot \ln(1-y)] \\ +[(1-x)\cdot \mu_{La}^{s,vib}(T) + x\cdot \mu_{Sr}^{s,vib}(T)] + [(y\cdot \mu_{Co}^{s,vib}(T) + (1-y)\cdot \mu_{Fe}^{s,vib}(T)] + 3\mu_{O}^{s,vib}(T) \end{array} \right\} \quad (18)$$

Now, considering the oxygen equilibrium between the perovskite phase and the O_2 gas phase, $\mu_O^{gas}(T,P) = \mu_O^{PV}(T)$, the sum of chemical potentials of metals in the perovskite can be written based on Equations (16) and (18):

$$[(1-x)\cdot \mu_{La}^{PV} + x\cdot \mu_{Sr}^{PV}] + [(y\cdot \mu_{Co}^{PV} + (1-y)\cdot \mu_{Fe}^{PV}]$$

$$= g(La_{1-x}Sr_xCo_yFe_{1-y}O_3) - 3\cdot \mu_O^{PV}(T)$$

$$= g(La_{1-x}Sr_xCo_yFe_{1-y}O_3) - 3\cdot \mu_O^{gas}(T,P)$$

$$= \begin{bmatrix} E^{DFT}(La_{1-x}Sr_xCo_yFe_{1-y}O_3) \\ +k\cdot T[x\cdot\ln(x)+(1-x)\cdot\ln(1-x)] \\ +k\cdot T[y\cdot\ln(y)+(1-y)\cdot\ln(1-y)] \\ +[(1-x)\cdot\mu_{La}^{s,vib}(T)+x\cdot\mu_{Sr}^{s,vib}(T)]+ \\ [(y\cdot\mu_{Co}^{s,vib}(T)+(1-y)\cdot\mu_{Fe}^{s,vib}(T)]+3\cdot\mu_O^{s,vib}(T) \end{bmatrix} - 3\cdot\mu_O^{gas}(T,P) \quad (19)$$

Following Equation (6), the $\mu_O^{s,vib}(T)$ and the $\mu_O^{gas}(T,P)$ terms can be replaced by the $\mu_O^{eff}(T,P)$, we then obtain:

$$[(1-x)\cdot\mu_{La}^{PV}+x\cdot\mu_{Sr}^{PV}]+[(y\cdot\mu_{Co}^{PV}+(1-y)\cdot\mu_{Fe}^{PV}]$$

$$= \begin{bmatrix} E^{DFT}(La_{1-x}Sr_xCo_yFe_{1-y}O_3) \\ +k\cdot T[x\cdot\ln(x)+(1-x)\cdot\ln(1-x)] \\ +k\cdot T[y\cdot\ln(y)+(1-y)\cdot\ln(1-y)] \\ +[(1-x)\cdot\mu_{La}^{s,vib}(T)+x\cdot\mu_{Sr}^{s,vib}(T)] \\ +[(y\cdot\mu_{Co}^{s,vib}(T)+(1-y)\cdot\mu_{Fe}^{s,vib}(T)] \end{bmatrix} - 3\cdot\mu_O^{eff}(T,P) \quad (20)$$

For the effective chemical potential expression of $La_{1-x}Sr_xCo_yFe_{1-y}O_3$ perovskites, we move the vibrational free energies terms for the metal constituents from the right-hand side to the left-hand side and Euqation 20 becomes:

$$[(1-x)\cdot\mu_{La}^{eff}+x\cdot\mu_{Sr}^{eff}]+[(y\cdot\mu_{Co}^{eff}+(1-y)\cdot\mu_{Fe}^{eff}]$$

$$\equiv[(1-x)\cdot(\mu_{La}^{PV}-\mu_{La}^{s,vib})+x\cdot(\mu_{Sr}^{PV}-\mu_{Sr}^{s,vib})]+[(y\cdot(\mu_{Co}^{PV}-\mu_{Co}^{s,vib})+(1-y)\cdot(\mu_{Fe}^{PV}-\mu_{Fe}^{s,vib})]$$

$$= \begin{bmatrix} E^{DFT}(La_{1-x}Sr_xCo_yFe_{1-y}O_3) \\ +k \cdot T[x \cdot \ln(x) + (1-x) \cdot \ln(1-x)] \\ +k \cdot T[y \cdot \ln(y) + (1-y) \cdot \ln(1-y)] \end{bmatrix} - 3 \cdot \mu_O^{eff}(T,P) \quad (20')$$

With the defined effective chemical potentials of the constituents in the perovskites described above as well as those in the binary metal oxides discussed in the previous section, a thermodynamic phase diagram can be constructed at a given T and P, as will be further described below.

d. Construction of the bulk perovskite stability diagram

In the following discussion, we focus on the $La_{1-x}Sr_xCoO_3$ system for the construction of the bulk stability diagram.

To prevent metal constituents (e.g. La) from leaving $La_{1-x}Sr_xCoO_3$ perovskites to form binary oxides (e.g. La_2O_3) at a given T and P (which sets the $\mu_O^{gas}(T,P)$), requires

$$\mu_{La}(La_{1-x}Sr_xCoO_3) \le \mu_{La}(La_2O_3) \quad (21)$$

Based on the assumption that the vibration contributions of metal in the binary metal oxides and perovskites are equal, the inequality equation (Equation (21)) can be expressed in terms of the effective chemical potential of metal:

$$\mu_{La}(La_{1-x}Sr_xCoO_3) \le \mu_{La}(La_2O_3)$$

$$\Rightarrow \mu_{La}^{eff}(La_{1-x}Sr_xCoO_3) + \mu_{La}^{s,vib} \le \mu_{La}^{eff}(La_2O_3) + \mu_{La}^{s,vib} \quad (22)$$

Similarly the inequality equations of the other metal chemical potentials in $La_{1-x}Sr_xCoO_3$ vs. their binary oxides can be written as follows:

$$\mu_{Sr}(La_{1-x}Sr_xCoO_3) \le \mu_{Sr}(SrO) \Rightarrow \mu_{Sr}^{eff}(La_{1-x}Sr_xCoO_3) \le \mu_{Sr}^{eff}(SrO) \quad (23)$$

$$\mu_{Co}(La_{1-x}Sr_xCoO_3) \le \mu_{Co}(Co_3O_4) \Rightarrow \mu_{Co}^{eff}(La_{1-x}Sr_xCoO_3) \le \mu_{Co}^{eff}(Co_3O_4) \quad (24)$$

In addition, to prevent precipitation of the lower order perovskite $LaCoO_3$ and brownmillerite $SrCoO_{2.5}$ from $La_{1-x}Sr_xCoO_3$ perovskites:

$$\mu_{La}(La_{1-x}Sr_xCoO_3) + \mu_{Co}(La_{1-x}Sr_xCoO_3) \le \mu_{La}(LaCoO_3) + \mu_{Co}(LaCoO_3)$$

$$\Rightarrow \mu_{La}^{eff}(La_{1-x}Sr_xCoO_3) + \mu_{Co}^{eff}(La_{1-x}Sr_xCoO_3) \le \mu_{La}^{eff}(LaCoO_3) + \mu_{Co}^{eff}(LaCoO_3) \quad (25)$$

$$\mu_{Sr}(La_{1-x}Sr_xCoO_3) + \mu_{Co}(La_{1-x}Sr_xCoO_3) \le \mu_{Sr}(SrCoO_{2.5}) + \mu_{Co}(SrCoO_{2.5})$$

$$\Rightarrow \mu_{Sr}^{eff}(La_{1-x}Sr_xCoO_3) + \mu_{Co}^{eff}(La_{1-x}Sr_xCoO_3) \le \mu_{Sr}^{eff}(SrCoO_{2.5}) + \mu_{Co}^{eff}(SrCoO_{2.5}) \quad (26)$$

Based on the inequality equations (Equations (22)~(26)), the defined effective chemical potentials, and the calculated *ab initio* total energies of the oxides including $La_{1-x}Sr_xCoO_3$, $LaCoO_3$, $SrCoO_{2.5}$, Co_3O_4, SrO, and La_2O_3, a bulk phase diagram can be constructed at a given *T*

and *P*, as shown in Fig. S10†. It is noted that for clarity the effective metal chemical potentials of the metal binary oxides (Co_3O_4 and SrO) are chosen as the metal references in Fig. S10†. Therefore, the effective chemical potentials of Co and Sr are represented by $\Delta\mu_{Co}^{eff}(La_{0.75}Sr_{0.25}CoO_3)$ and $\Delta\mu_{Sr}^{eff}(La_{0.75}Sr_{0.25}CoO_3)$, where $\Delta\mu_{Co}^{eff}(La_{0.75}Sr_{0.25}CoO_3) = \mu_{Co}^{eff}(La_{0.75}Sr_{0.25}CoO_3) - \mu_{Co}^{eff}(Co_3O_4)$ and $\Delta\mu_{Sr}^{eff}(La_{0.75}Sr_{0.25}CoO_3) = \mu_{Sr}^{eff}(La_{0.75}Sr_{0.25}CoO_3) - \mu_{Sr}^{eff}(SrO)$.

e. $La_{0.75}Sr_{0.25}CoO_3$ surface stability analysis:

Surface calculations are performed using the 9-layer 2×2 symmetric (001) AO terminated and BO_2 terminated slabs with the composition of central 5 layers fixed to the bulk $La_{0.75}Sr_{0.25}CoO_3$. The La/Sr content of the top two and bottom two layers are varied, as illustrated in Fig. S11†. The chosen thickness of the adopted slab model is based on the convergence test for the surface energy vs. thickness of the asymmetric and symmetric slab models, where for mixed ionic and electronic conducting perovskites, it was observed that the 9-layer symmetric slab model is sufficient to give converged surface energy, surface charge doping, and surface defect energetics.[29] A total of 10 configurations (5 for the (001) AO surfaces and 5 for the (001) BO_2 surfaces) are calculated based on the 9-layer 2×2 symmetric slab model for the $La_{0.75}Sr_{0.25}CoO_3$ (001) surface stability analysis.

Surface stability analysis is performed using the following equation for calculating surface energy, Γ_i:

$$\Gamma_i = \frac{1}{2A_s}\left[\begin{array}{l} E_{total}^{slab} + N_A \cdot k \cdot T[x \cdot \ln(x) + (1-x) \cdot \ln(1-x)] + N_B \cdot k \cdot T[y \cdot \ln(y) + (1-y) \cdot \ln(1-y)] \\ -N_O \cdot \mu_O^{eff}(T,P) - (\sum_{j=La,Sr,Co}^{j-1} N_j \cdot \mu_j^{eff}) - N_R \cdot \mu_R^{eff} \end{array}\right] \quad (27)$$

where A_s is the surface area of the simulated 9-layer 2×2 slab (a factor of 2 in front of A_s is to account for two surface terminations in the symmetric slabs), E_{total}^{slab} is the total energy of the slab, N_A, N_B, and N_O are the number of A-site, B-site and oxygen site in the 9-layer symmetric slab, $\mu_O^{eff}(T,P)$ is the effective chemical potential of oxygen referenced to the O_2 gas phase at the standard condition (room temperature and 1 atm partial pressure of oxygen, T is temperature, P is the partial pressure of oxygen, N_j and N_R are the numbers of metal cations in the 9-layer symmetric slab, j denotes the specified (independent) metal constituents in the perovskite, R denotes the remaining (dependent) metal constituent that is not among the specified j metal constituents in the perovskite. μ_j^{eff} is the effective chemical potentials of specified (independent) metal j in the perovskite (relative to the chosen metal references, in this work, the chosen metal references are the effective chemical potentials of metals in the metal binary oxides) while μ_R^{eff} is the resulting (dependent) effective chemical potential of metal R set by the total energy of the bulk $La_{0.75}Sr_{0.25}CoO_3$ and the specified effective chemical potentials of μ_j^{eff}. For example, when μ_{Sr}^{eff} and μ_{Co}^{eff} are specified, μ_{La}^{eff} can be determined using Equation 20' and the calculated DFT total energy of $La_{0.75}Sr_{0.25}CoO_3$.

With the defined effective chemical potentials of the constituents for $La_{0.75}Sr_{0.25}CoO_3$, the surface energy can be obtained through Equation (27), and the calculated surface energy results are provided in Table S2† for the condition of T = 550 ºC and $p(O_2)$ = 1 atm. By comparing the calculated surface energies of the investigated $La_{0.75}Sr_{0.25}CoO_3$ surface configurations, the surface Sr composition of the surface termination (AO or BO_2) with the lowest surface energy is presented by the contour plot shown in Fig. S12†. The *ab initio* thermodynamic analysis results suggest the most stable (001) surfaces within the bulk $La_{0.75}Sr_{0.25}CoO_3$ region is the AO surface termination with Sr concentration of 0.75 at T = 550 ºC and $p(O_2)$ = 1 atm. In addition, further increasing $p(O_2)$ to 50 atm, the stable bulk LSC_{113} region spans on both the AO surface with 75% and 100% Sr concentration on the A site as the most stable (001) surface, while decreasing $p(O_2)$ to 0.05 atm, the stable bulk LSC_{113} region is moved farther apart from the chemical potential region where the fully Sr-enriched AO surface is the stable (001) surface, as shown in Fig. S12b† and S12c†. The $p(O_2)$ dependence of the LSC_{113} surface stability analysis suggests that the (001) AO surface with higher Sr content can be stabilized by increasing $p(O_2)$, consistent with the reported $p(O_2)$ dependence in surface Sr enrichment of Sr-doped $LaMnO_3$ and $LSCF_{113}$ perovskites.[36, 37]. Particularly, the increase of the driving force for perovskite surface Sr segregation upon increasing $p(O_2)$ was proposed to be associated with electrostatic interactions based on the DFT and analytic models for Sr dopant interaction with charged cation and oxygen vacancies, as stability of cation and oxygen vacancies also exhibits $p(O_2)$ dependences.[36] Since no cation and anion vacancies were included in our slab models, our thermodynamic analysis suggests that enhanced perovskite surface Sr segregation upon increasing $p(O_2)$ can be attributed to minimizing surface free energy in responding to relative metal chemical potential change in

bulk perovskites upon change of oxygen chemical potential, in contrast to dopant-point defect interactions.

f. $La_{0.625}Sr_{0.375}Fe_{0.75}Co_{0.25}O_3$ and $LaSrCoO_4$ surface stability analysis:

The same *ab initio* thermodynamic analysis performed on the $La_{0.75}Sr_{0.25}CoO_3$ surfaces can also be extended to the $La_{0.625}Sr_{0.375}Fe_{0.75}Co_{0.25}O_3$ (001) surfaces as well as the LSC_{214} (001) and (100) surfaces, although the number of the independent (chemical potential) degree of freedom is three for $La_{0.625}Sr_{0.375}Fe_{0.75}Co_{0.25}O_3$, which will make the bulk stability diagram three-dimensional. In Fig. S13†, we show the results of the predicted surface stability diagram at selected effective chemical potentials of Fe in $La_{0.625}Sr_{0.375}Fe_{0.75}Co_{0.25}O_3$ (relative to the effective chemical potential of Fe in Fe_2O_3), based on the investigated 50 (001) slab configurations (25 for the (001) AO surfaces and 25 for the (001) BO_2 surfaces) in the DFT calculations. The *ab initio* thermodynamic analysis results suggest the most stable (001) surfaces within the stable bulk $La_{0.625}Sr_{0.375}Fe_{0.75}Co_{0.25}O_3$ region (relative to the lower order oxides, $LaFeO_3$, $SrFeO_{2.5}$, $LaCoO_3$, $SrCoO_{2.5}$, Co_3O_4, Fe_2O_3, SrO, and La_2O_3) is the AO surface termination with Sr concentration of 1.00.

Fig. S14† shows the contour plots for the LSC_{214} stable surface composition vs. chemical potential of metals (here we chose μ(Sr) in SrO/LSC_{214} equilibrium and μ(Co) in Co_3O_4/LSC_{214} equilibrium as the metal chemical potential references) within the stability boundary of bulk LSC_{214} in equilibrium with La_2O_3, SrO, Co_3O_4, $LaCoO_3$, and $SrCoO_{2.5}$ based on the most stable surface energy of the investigated 6 LSC_{214} slab configurations at (a) T = 550 ºC and $p(O_2)$ = 1 atm. The boundary lines in Fig. S14† are for LSC_{214} bulk stability, while the contour colormap represents the most stable surface configurations among the investigated DFT slab models. As

shown in Fig. S14†, our *ab initio* thermodynamic analysis predicts the fully Sr enriched (001) AO surface is the most stable surface among the investigated (100) AO surface and (100) A_2BO_4 surface configurations within the bulk LSC_{214} stability region at $p(O_2)$ = 1 atm and T = 550 ºC (shaded region), while both the (001) AO and the (100) A_2BO_4 surfaces are predicted to be stable with fully enriched surface layer Sr at the A-sites within the same surface orientation. Comparatively, the surface energy of the fully Sr-enriched (100) A_2BO_4 surface is found to be a factor of 1.2 ~ 2 greater than the surface energy of the fully Sr-enriched (001) AO surface within the stable bulk $LaSrCoO_4$ region.

References

1. M. Pechini, *U.S. Patent No. 3,330,697*, 1967.
2. H. M. Christen, E. D. Specht, S. S. Silliman and K. S. Harshavardhan, *Phys. Rev. B*, 2003, **68**, 4.
3. E. J. Crumlin, E. Mutoro, Z. Liu, M. E. Grass, M. D. Biegalski, Y. L. Lee, D. Morgan, H. M. Christen, H. Bluhm and Y. Shao-Horn, *Energy Environ. Sci.*, 2012, **5**, 6081-6088.
4. G. J. la O, S. J. Ahn, E. Crumlin, Y. Orikasa, M. D. Biegalski, H. M. Christen and Y. Shao-Horn, *Angew. Chem.-Int. Edit.*, 2010, **49**, 5344-5347.
5. S. B. Adler, *Chem. Rev.*, 2004, **104**, 4791-4843.
6. S. B. Adler, J. A. Lane and B. C. H. Steele, *J. Electrochem. Soc.*, 1996, **143**, 3554-3564.
7. T. Kawada, J. Suzuki, M. Sase, A. Kaimai, K. Yashiro, Y. Nigara, J. Mizusaki, K. Kawamura and H. Yugami, *J. Electrochem. Soc.*, 2002, **149**, E252-E259.
8. Y. L. Yang, C. L. Chen, S. Y. Chen, C. W. Chu and A. J. Jacobson, *J. Electrochem. Soc.*, 2000, **147**, 4001-4007.
9. P. S. Manning, J. D. Sirman, R. A. DeSouza and J. A. Kilner, *Solid State Ion.*, 1997, **100**, 1-10.
10. J. Maier, *Solid State Ionics*, 1998, **112**, 197-228.
11. J. Maier, *Physical Chemistry of Ionic Materials: Ions and Electrons in Solids* John Wiley, Chichester, England ; Hoboken, NJ, 2004.
12. J. Fleig and J. Maier, *J. Eur. Ceram. Soc.*, 2004, **24**, 1343-1347.
13. S. Hashimoto, Y. Fukuda, M. Kuhn, K. Sato, K. Yashiro and J. Mizusaki, *Solid State Ion.*, 2011, **186**, 37-43.
14. R. A. De Souza and J. A. Kilner, *Solid State Ion.*, 1999, **126**, 153-161.

15. J. Fleig, H. R. Kim, J. Jamnik and J. Maier, *Fuel Cells*, 2008, **8**, 330-337.

16. J. Fleig, *Solid State Ion.*, 2002, **150**, 181-193.

17. G. Kresse and J. Hafner, *Phys. Rev. B*, 1993, **47**, 558.

18. G. Kresse and J. Furthmuller, *Phys. Rev. B*, 1996, **54**, 11169-11186.

19. P. E. Blochl, *Phys. Rev. B*, 1994, **50**, 17953-17979.

20. J. P. Perdew and Y. Wang, *Phys. Rev. B*, 1992, **45**, 13244.

21. V. I. Anisimov, F. Aryasetiawan and A. I. Lichtenstein, *J. Phys.: Condens. Matter*, 1997, **9**, 767-808.

22. S. L. Dudarev, G. A. Botton, S. Y. Savrasov, C. J. Humphreys and A. P. Sutton, *Phys. Rev. B*, 1998, **57**, 1505-1509.

23. M. J. Gadre, Y. L. Lee and D. Morgan, *Phys. Chem. Chem. Phys.*, 2012, **14**, 2606-2616.

24. Y.-L. Lee, J. Kleis, J. Rossmeisl and D. Morgan, *Phys. Rev. B: Condens. Matter Mater. Phys.*, 2009, **80**, 224101.

25. K. Johnston, M. R. Castell, A. T. Paxton and M. W. Finnis, *Phys. Rev. B*, 2004, **70**, 085415.

26. S. Piskunov, E. Heifets, T. Jacob, E. A. Kotomin, D. E. Ellis and E. Spohr, *Phys. Rev. B*, 2008, **78**, 121406(R).

27. NIST, in *NIST Standard Reference Database No. 69,* http://webbook.nist.gov/chemistry/, eds. P. J. Linstrom and W. G. Mallard, National Institute of Standards and Technology, Gaithersburg, MD, 2003.

28. K. Reuter and M. Scheffler, *Phys. Rev. B*, 2001, **65**, 035406.

29. Y. L. Lee, Y. Shao-Horn and D. Morgan, *Under Review*, 2014

30. J. Leitner, P. Chuchvalec, D. Sedmidubský, A. Strejc and P. Abrman, *Thermochimica Acta*, 2002, **395**, 27-46.

31. Y.-L. Lee and D. Morgan, *Phys. Chem. Chem. Phys.*, 2012, **14**, 290-302.

32. L. Wang, T. Maxisch and G. Ceder, *Phys. Rev. B*, 2006, **73**, 195107.

33. J. Cheng, A. Navrotsky, X.-D. Zhou and H. U. Anderson, *Chem. Mater.*, 2005, **17**, 2197-2207.

34. J. H. Cheng, A. Navrotsky, X. D. Zhou and H. U. Anderson, *J. Mater. Res.*, 2005, **20**, 191-200.

35. T. R. S. Prasanna and A. Navrotsky, *J. Solid State Chem.*, 1994, **112**, 192-195.

36. W. Lee, J. W. Han, Y. Chen, Z. H. Cai and B. Yildiz, *J. Am. Chem. Soc.*, 2013, **135**, 7909-7925.

37. D. Oh, D. Gostovic and E. D. Wachsman, *J. Mater. Res.*, 2012, **27**, 1992-1999.

Table S1. The calculated *ab initio* oxide formation energies vs. the experimentally measured oxide formation enthalpies from the literature [33-35] for the LSF_{113}, LSC_{113}, and LSC_{214} perovskites related compounds.

Perovskite phase	Reactants in the Oxide Formation Reaction	DFT (eV/F.U.)	Exp. (eV/F.U.)	Difference (eV/FU)
$LaFeO_3$ (GAFM)	La_2O_3, Fe_2O_3	-0.525	-0.669 [33]	0.144
$La_{0.75}Sr_{0.25}FeO_3$ (GAFM)	La_2O_3, SrO, Fe_2O_3, O_2	-0.563	-0.652** [33]	0.089
$La_{0.5}Sr_{0.5}FeO_3$ (FM*)	La_2O_3, SrO, Fe_2O_3, O_2	-0.590	-0.664 [33]	0.074
$SrFeO_{2.5}$ (FM)	SrO, Fe_2O_3, O_2	-0.484	-0.483 [33]	-0.001
$SrFeO_3$ (FM)	SrO, Fe_2O_3, O_2	-0.935	--	--
$LaCoO_3$ (FM)	La_2O_3, CoO, O_2	-0.957	-1.115 [34]	0.158
$La_{0.75}Sr_{0.25}CoO_3$ (FM)	La_2O_3, SrO, CoO, O_2	-1.061	--	--
$SrCoO_{2.5}$ (FM)	SrO, CoO, O_2	-1.032	--	--
$La_{1.25}Sr_{0.75}CoO_4$ (FM)	La_2O_3, SrO, CoO, O_2	-0.964	-1.047 [35]	0.083
$LaSrCoO_4$ (FM)	La_2O_3, SrO, CoO, O_2	-1.243	-1.219 [35]	-0.024
$La_{0.75}Sr_{1.25}CoO_4$ (FM)	La_2O_3, SrO, CoO, O_2	-1.308	-1.304 [35]	-0.04
$SrCo_{0.25}Fe_{0.75}O_3$ (FM)	SrO, Fe_2O_3, Co_3O_4, O_2	-0.838	--	--
$SrCoO_3$ (FM)	SrO, Co_3O_4, O_2	-0.582	--	--
Sr_2CoO_4 (FM)	SrO, Co_3O_4, O_2	-0.967	--	--

* FM is more stable than GAFM
**values are from interpolation of the data between two nearest Sr concentration.

Table S2. The calculated surface energy results at the chemical potential grid shown in Fig. S12a†. The cells in the yellow background represent the most stable surface energy among those of the investigated configurations.

	$\Delta\mu^{eff}_{Sr}$ (LSC_{113})	0.000 eV		-0.055 eV		-0.110 eV		-0.165 eV		-0.219 eV		-0.274 eV		-0.329 eV		-0.384 eV		-0.439 eV		-0.494 eV		-0.549 eV	
$\Delta\mu^{eff}_{Co}$ (LSC_{113})	meV/Å²	AO	BO_2	AO	BO_2	AO	BO_2	AO	BO_2	AO	BO_2	AO	BO_2	AO	BO_2	AO	BO_2	AO	BO_2	AO	BO_2	AO	BO_2
0.0 eV	Sr=0.0	80.753	75.013	79.547	73.807	78.341	72.601	77.135	71.395	75.929	70.189	74.723	68.983	73.517	67.778	72.311	66.572	71.106	65.366	69.900	64.160	68.694	62.954
	Sr=0.25	55.719	66.116	55.719	66.116	55.719	66.116	55.719	66.116	55.719	66.116	55.719	66.116	55.719	66.116	55.719	66.116	55.719	66.116	55.719	66.116	55.719	66.116
	Sr=0.5	39.384	69.262	40.590	70.468	41.796	71.674	43.002	72.879	44.208	74.085	45.414	75.291	46.620	76.497	47.826	77.703	49.031	78.909	50.237	80.115	51.443	81.321
	Sr=0.75	21.772	65.637	24.184	68.049	24.184	70.461	29.007	72.872	**31.419**	75.284	**33.831**	77.696	**36.243**	80.108	**38.654**	82.519	**41.066**	84.931	**43.478**	87.343	**45.890**	89.755
	Sr=1.0	**17.452**	63.834	**21.069**	67.451	**21.069**	71.069	**28.304**	67.451	31.922	78.304	35.540	81.922	39.157	85.539	42.775	89.157	46.393	92.775	50.010	96.392	53.628	100.010
-0.014 eV	Sr=0.0	79.999	75.164	78.793	73.958	77.587	72.752	76.381	71.546	75.175	70.340	73.970	69.134	72.764	67.928	71.558	66.722	70.352	65.517	69.146	64.311		
	Sr=0.25	55.267	66.568	55.267	66.568	55.267	66.568	55.267	66.568	55.267	66.568	55.267	66.568	55.267	66.568	55.267	66.568	55.267	66.568	55.267	66.568		
	Sr=0.5	39.234	70.015	40.440	71.221	41.645	72.427	42.851	73.633	44.057	74.839	45.263	76.045	46.469	77.251	47.675	78.457	48.881	79.662	50.087	80.868		
	Sr=0.75	21.923	66.692	24.334	69.104	26.746	71.516	29.158	73.927	**31.570**	76.339	**33.982**	78.751	**36.393**	81.163	**38.805**	83.574	**41.217**	85.986	**43.629**	88.398		
	Sr=1.0	**17.904**	65.190	**21.521**	68.808	**25.139**	72.425	**28.757**	76.043	32.374	79.661	35.992	83.278	39.610	86.896	43.227	90.514	46.845	94.131	50.462	97.749		
-0.027 eV	Sr=0.0	79.245	75.314	78.039	74.108	76.834	72.903	75.628	71.697	74.422	70.491	73.216	69.285	72.010	68.079	70.804	66.873	69.598	65.667				
	Sr=0.25	54.815	67.020	54.815	67.020	54.815	67.020	54.815	67.020	54.815	67.020	54.815	67.020	54.815	67.020	54.815	67.020	54.815	67.020				
	Sr=0.5	39.083	70.769	40.289	71.975	41.495	73.181	42.701	74.387	43.906	75.593	45.112	76.798	46.318	78.004	47.524	79.210	48.730	80.416				
	Sr=0.75	22.073	67.747	24.485	70.159	26.897	72.571	29.309	74.983	**31.720**	77.394	**34.132**	79.806	**36.544**	82.218	**38.956**	84.630	**41.368**	87.041				
	Sr=1.0	**18.356**	66.547	**21.974**	70.164	**25.591**	73.782	**29.209**	77.400	32.826	81.017	36.444	84.635	40.062	88.253	43.679	91.870	47.297	95.488				
-0.041 eV	Sr=0.0	78.492	75.465	77.286	74.259	76.080	73.053	74.874	71.847	73.668	70.641	72.462	69.436	71.256	68.230	70.050	67.024						
	Sr=0.25	54.362	67.473	54.362	67.473	54.362	67.473	54.362	67.473	54.362	67.473	54.362	67.473	54.362	67.473	54.362	67.473						
	Sr=0.5	38.932	71.523	40.138	72.729	41.344	73.935	42.550	75.140	43.756	76.346	44.962	77.552	46.167	78.758	47.373	79.964						
	Sr=0.75	22.224	68.802	24.636	71.214	27.048	73.626	**29.459**	76.038	**31.871**	78.449	**34.283**	80.861	**36.695**	83.273	**39.106**	85.685						
	Sr=1.0	**18.808**	67.903	**22.426**	71.521	**26.043**	75.139	29.661	78.756	33.279	82.374	36.896	85.992	40.514	89.609	44.132	93.227						
-0.055 eV	Sr=0.0	77.738	75.616	76.532	74.410	75.326	73.204	74.120	71.998	72.914	70.792	71.709	69.586	70.503	68.380								
	Sr=0.25	53.910	67.925	53.910	67.925	53.910	67.925	53.910	67.925	53.910	67.925	53.910	67.925	53.910	67.925								
	Sr=0.5	38.781	72.276	39.987	73.482	41.193	74.688	42.399	75.894	43.605	77.100	44.811	78.306	46.017	79.512								
	Sr=0.75	22.375	69.858	24.787	72.269	27.198	74.681	**29.610**	77.093	**32.022**	79.505	**34.434**	81.916	**36.845**	84.328								
	Sr=1.0	**19.260**	69.260	**22.878**	72.878	**26.496**	76.495	30.113	80.113	33.731	83.731	37.349	87.348	40.966	90.966								
-0.069 eV	Sr=0.0	76.984	75.766	75.778	74.561	74.572	73.355	73.367	72.149	72.161	70.943	70.955	69.737										
	Sr=0.25	53.458	68.377	53.458	68.377	53.458	68.377	53.458	68.377	53.458	68.377	53.458	68.377										
	Sr=0.5	38.631	73.030	39.837	74.236	41.043	75.442	42.248	76.648	43.454	77.854	44.660	79.060										
	Sr=0.75	22.526	70.913	24.937	73.324	27.349	75.736	**29.761**	78.148	**32.173**	80.560	**34.584**	82.972										
	Sr=1.0	**19.713**	70.617	**23.330**	74.234	**26.948**	77.852	30.565	81.469	34.183	85.087	37.801	88.705										
-0.082 eV	Sr=0.0	76.231	75.917	75.025	74.711	73.819	73.505	72.613	72.300	71.407	71.094												
	Sr=0.25	53.006	68.829	53.006	68.829	53.006	68.829	53.006	68.829	53.006	68.829												
	Sr=0.5	38.480	73.784	39.686	74.990	40.892	76.196	42.098	77.401	43.304	78.607												
	Sr=0.75	22.676	71.968	25.088	74.380	27.500	76.791	**29.912**	79.203	**32.323**	81.615												
	Sr=1.0	**20.165**	71.973	**23.782**	75.591	**27.400**	79.208	31.018	82.826	34.635	86.444												
-0.096 eV	Sr=0.0	75.477	76.068	74.271	74.862	73.065	73.656	71.859	72.450														
	Sr=0.25	52.554	69.281	52.554	69.281	52.554	69.281	52.554	69.281														
	Sr=0.5	38.329	74.537	39.535	75.743	40.741	76.949	41.947	78.155														
	Sr=0.75	22.827	73.023	25.239	75.435	**27.651**	77.847	**30.062**	80.258														
	Sr=1.0	**20.617**	73.330	**24.235**	76.947	27.852	80.565	31.470	84.183														
-0.110 eV	Sr=0.0	74.723	76.219	73.517	75.013	72.311	73.807																
	Sr=0.25	52.101	69.734	52.101	69.734	52.101	69.734																
	Sr=0.5	38.179	75.291	39.384	76.497	40.590	77.703																
	Sr=0.75	22.978	74.078	25.390	76.490	**27.801**	78.902																
	Sr=1.0	**21.069**	74.686	**24.687**	78.304	28.304	81.922																
-0.123 eV	Sr=0.0	73.970	76.369	72.764	75.164																		
	Sr=0.25	51.649	70.186	51.649	70.186																		
	Sr=0.5	38.028	76.045	39.234	77.251																		
	Sr=0.75	23.129	75.133	25.540	77.545																		
	Sr=1.0	**21.521**	76.043	**25.139**	79.661																		
-0.137 eV	Sr=0.0	73.216	76.520																				
	Sr=0.25	51.197	70.638																				
	Sr=0.5	37.877	76.798																				
	Sr=0.75	23.279	76.188																				
	Sr=1.0	**21.974**	77.400																				

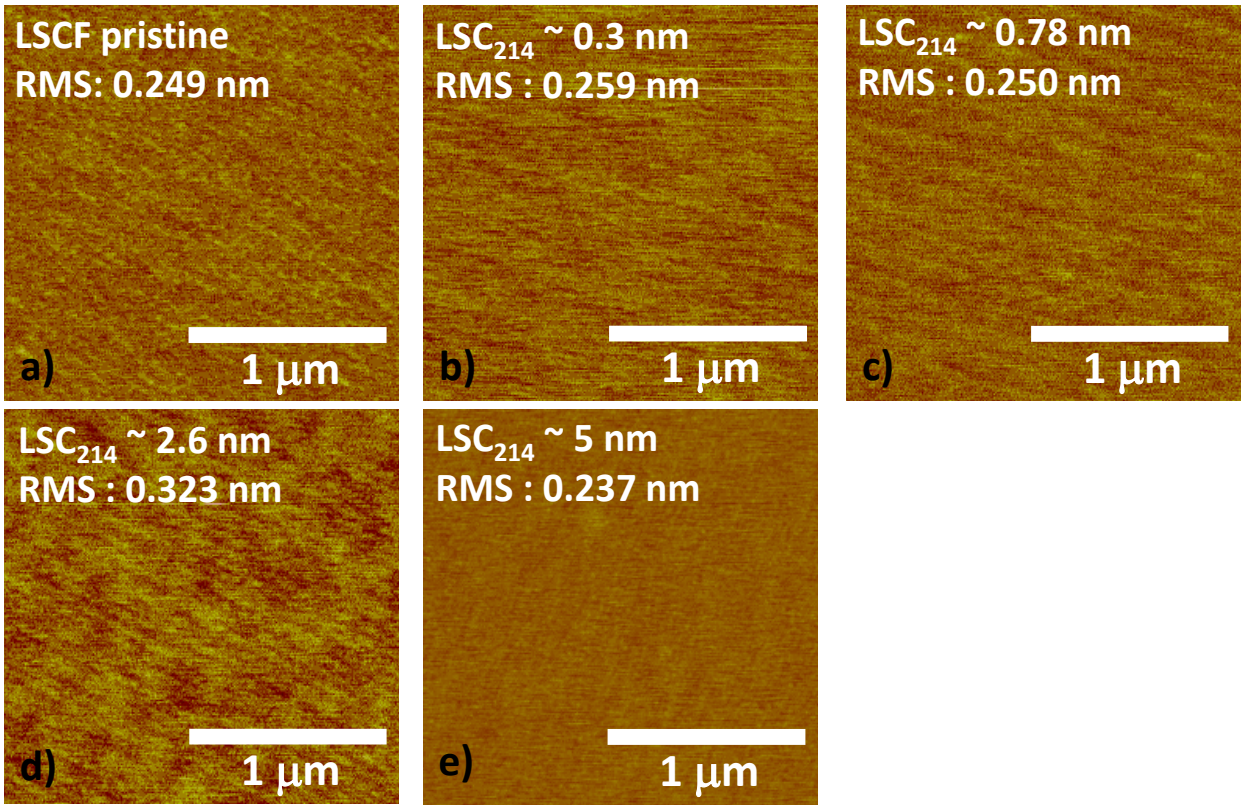

Fig. S1. AFM images of (a) as-deposited pristine $LSCF_{113}$ ~63 nm, (b) $LSCF_{113}$ with ~0.3 nm LSC_{214}, (c) $LSCF_{113}$ with ~0.8 nm LSC_{214}, (d) $LSCF_{113}$ with ~2.6 nm LSC_{214}, and (e) $LSCF_{113}$ with ~5 nm LSC_{214}. RMS roughness values were in the range of 0.24 – 0.32 nm and comparable across all surfaces.

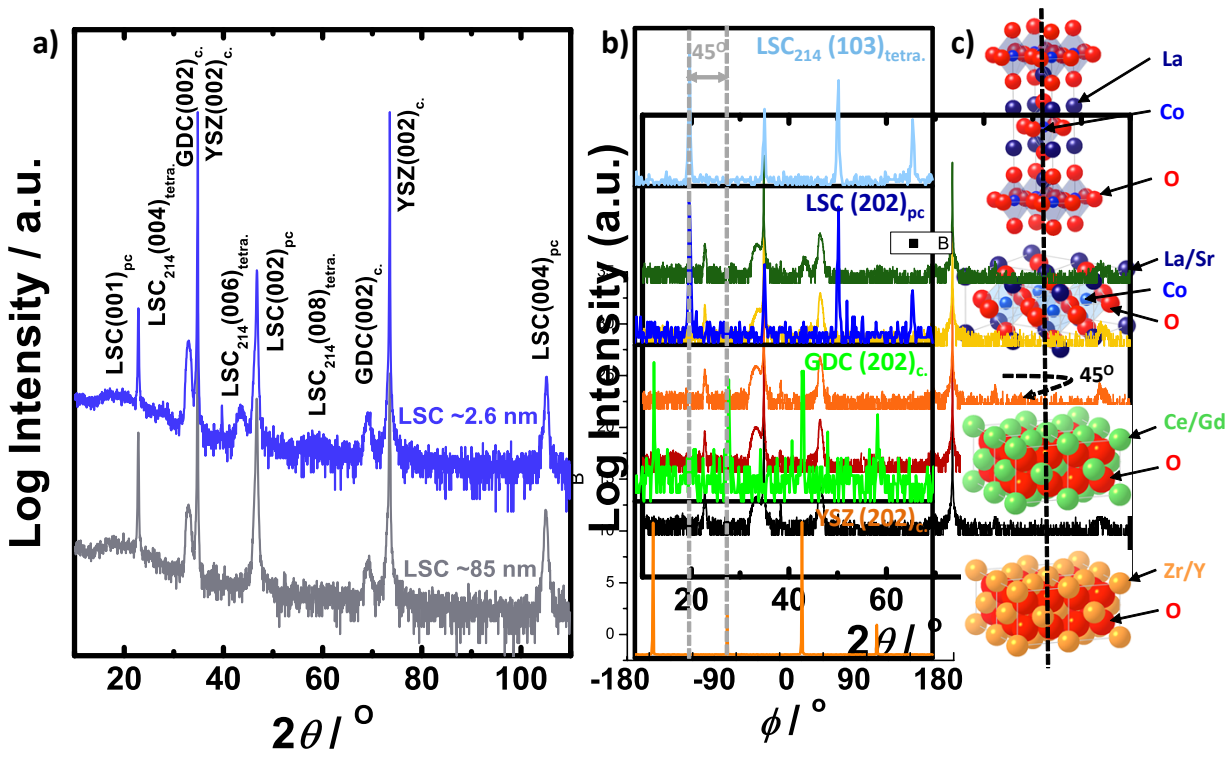

Fig. S2. X-ray diffraction (Cu K_α) analysis at room temperature. (a) Normal XRD of the epitaxial LSC_{113} reference and the LSC_{214}-decorated LSC_{113} film, (b) off-normal XRD of a similarly prepared sample with a ~2.6 nm LSC_{214} coverage, and (c) schematic of the crystallographic rotational relationships among the $LSC_{214}(001)_{tetra.}$, $LSC_{113}(001)_{pc}$, $GDC(001)_{cubic}$, and $YSZ(001)_{cubic}$.

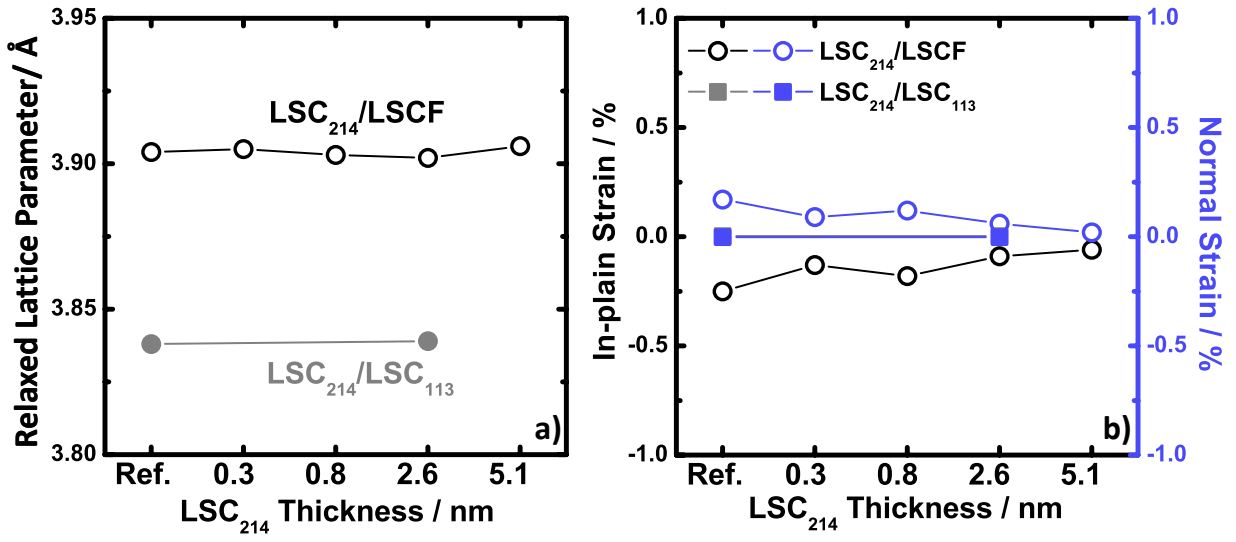

Fig. S3. (a) Relaxed lattice parameters of both $LSCF_{113}$ and LSC_{113} as a function of LSC_{214} thickness, calculated from HRXRD data. (b) In-plain and out-of-plane strains of both $LSCF_{113}$ and LSC_{113} as a function of LSC_{214} thickness, calculated from HRXRD data.

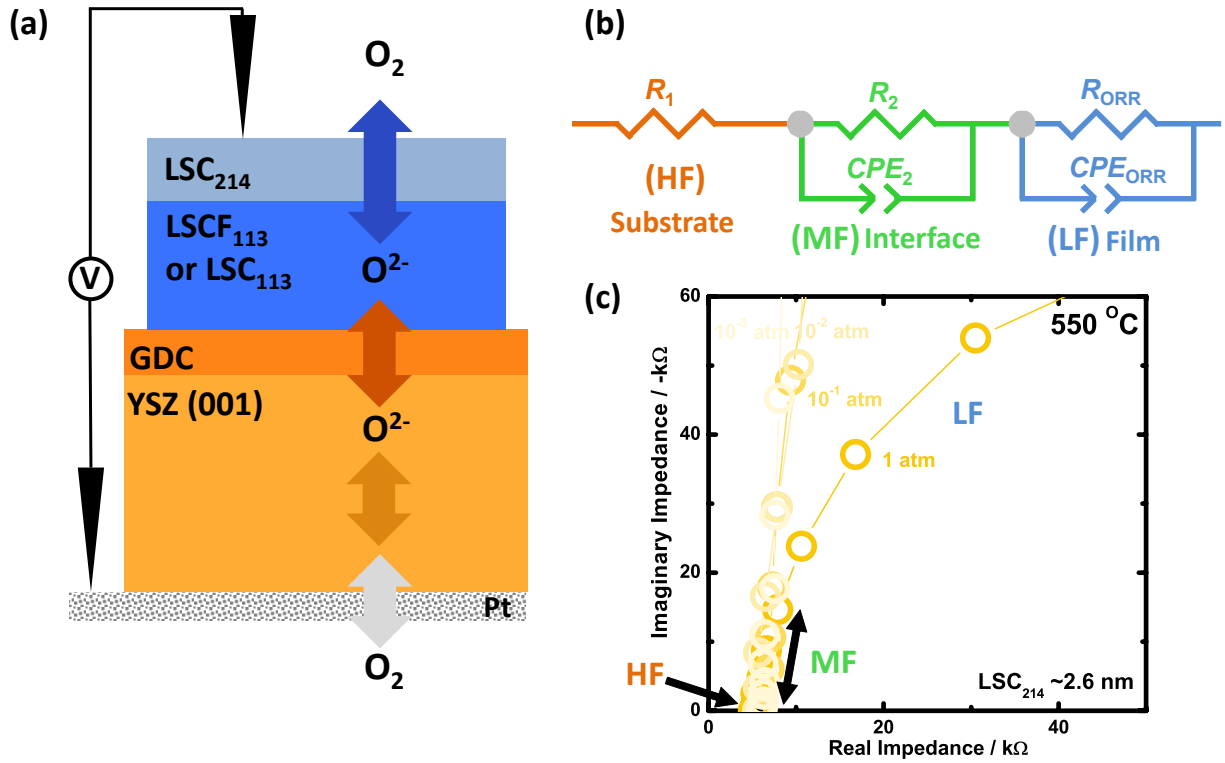

Fig. S4. (a) Schematic of a $LSC_{214}/LSCF_{113}$ or LSC_{113}/GDC/YSZ(001)/porous Pt sample and electrochemical testing configuration (not drawn to scale), and (b) equivalent circuit (R_1 = YSZ electrolyte resistance, R_2 = electrode/electrolyte interface resistance[4], R_{ORR} = ORR resistance, CPE = constant phase element) used to extract ORR kinetics, and (c) Nyquist plot of the epitaxial $LSCF_{113}$ with ~2.6 nm LSC_{214} coverage at 550 ^{O}C; inset shows a magnification (HF: $10^4 \sim 10^5$ Hz, MF: $10^3 \sim 10^4$ Hz, and LF: $10^{-2} \sim 10^3$ Hz).

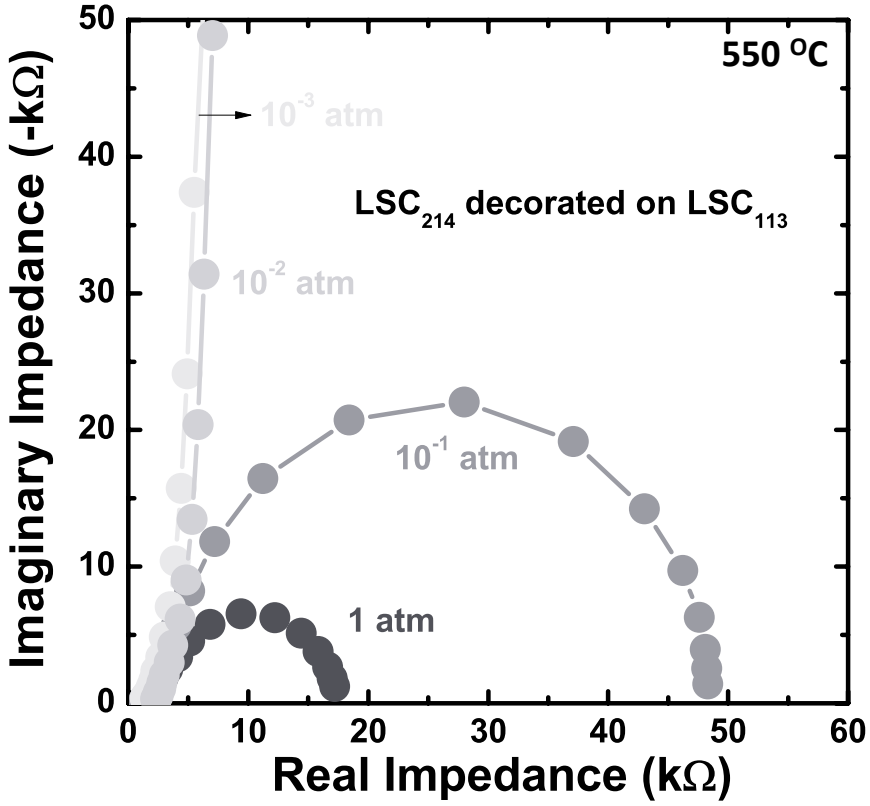

Fig. S5. Nyquist plot of the epitaxial LSC_{214}-decorated LSC_{113} thin film as a function of oxygen partial pressure at 550 ^{O}C. EIS data of the LSC_{214}-decorated LSC_{113} was found to show the $p(O_2)$-dependent impedance responses, which suggest that the oxygen surface exchange kinetics governs the oxygen electrocatalysis on the film surface.[5]

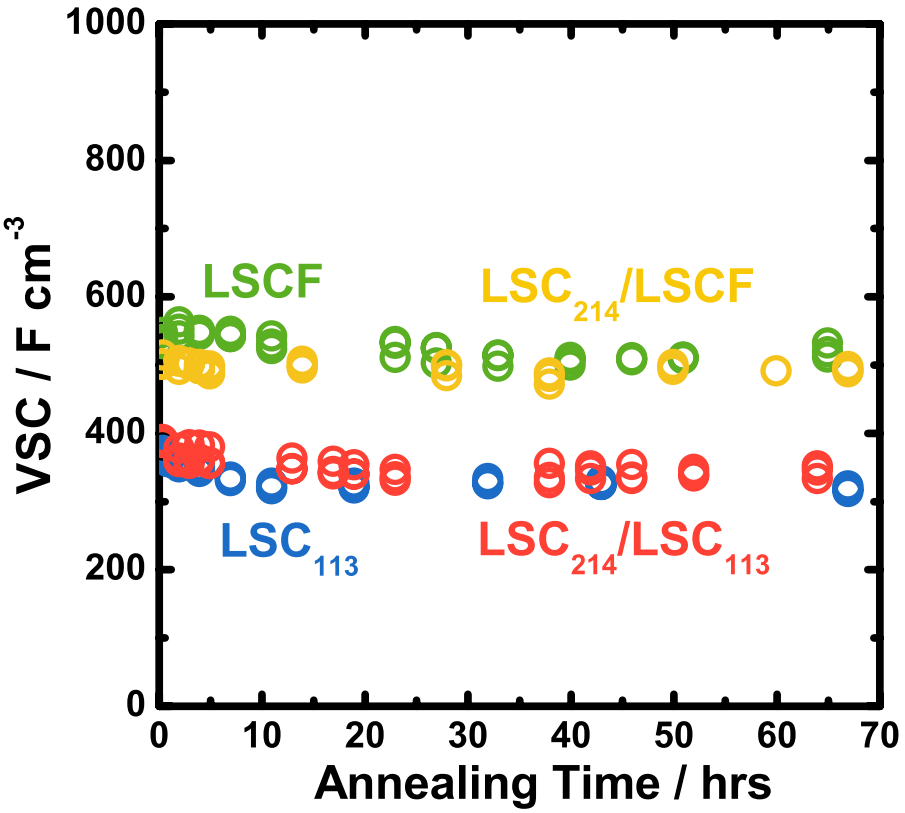

Fig. S6. Time-dependent volume specific capacitance (*VSC*) of the epitaxial $LSCF_{113}$, LSC_{113}, LSC_{214}-decorated $LSCF_{113}$, and LSC_{214}-decorated LSC_{113} films calculated from EIS spectra collected at 550 ºC with an oxygen partial pressure of 1 atm.

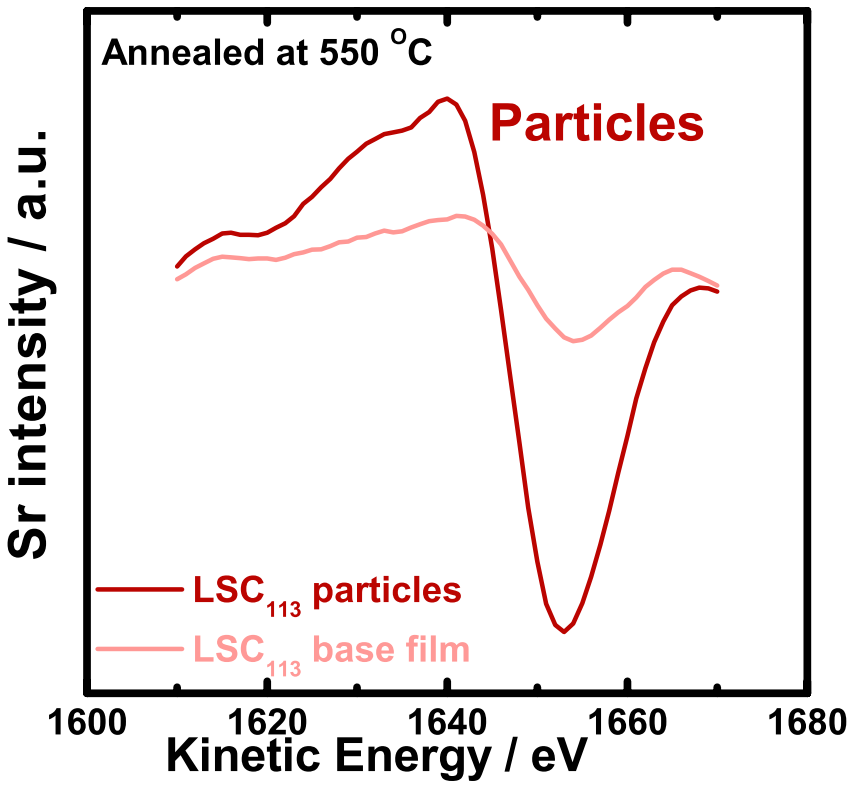

Fig. S7. Sr Auger spectra for the undecorated LSC_{113} thin film after annealing at 550 ^{O}C for 6 hours. Observed particles on the surface of LSC_{113} shows higher Sr peak intensity compared to the rest of the film surface.

(a) $La_{0.625}Sr_{0.375}Fe_{0.75}Co_{0.25}O_3$

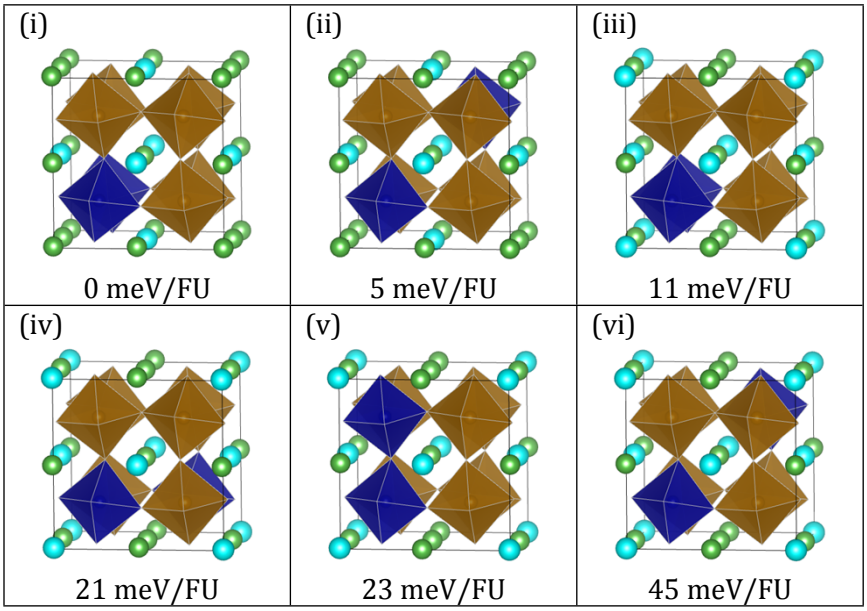

(b) $La_{0.5}Sr_{0.5}Fe_{0.75}Co_{0.25}O_3$

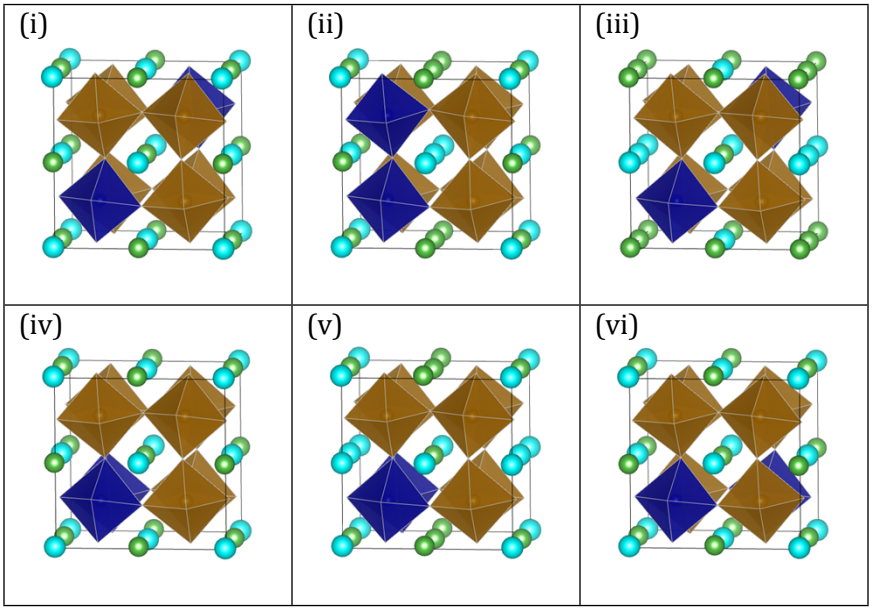

(c) $(La_{0.5}Sr_{0.5})_2CoO_4$

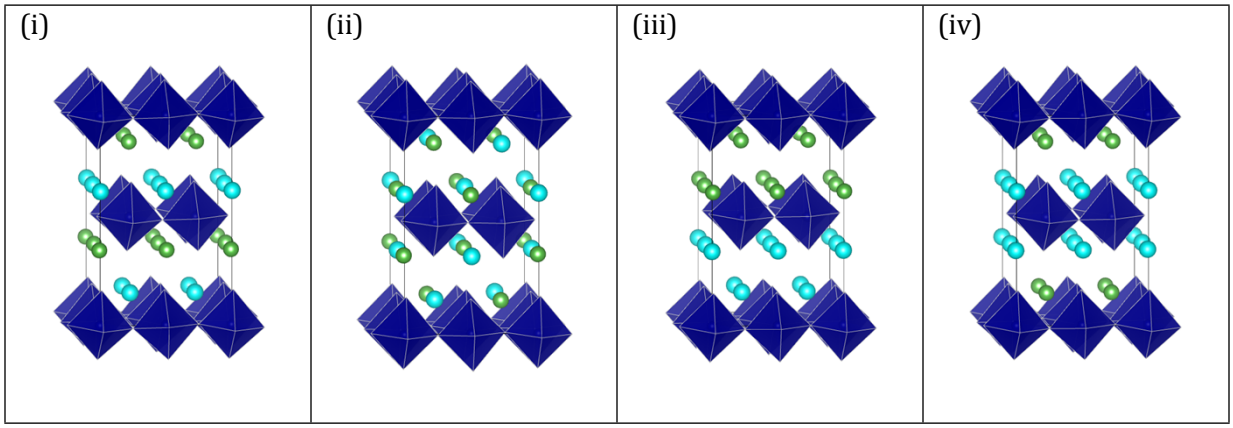

(d) $(La_{0.4375}Sr_{0.5625})_2CoO_4$

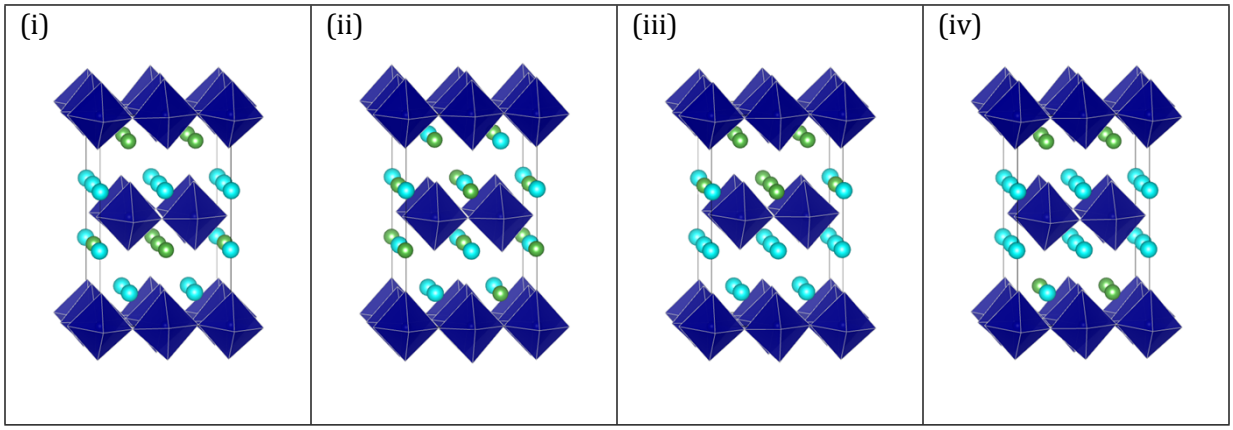

Fig. S8. Simulated $LSCF_{113}$ and LSC_{214} configurations for calculating the energies of Sr substitution of La (Sr_{La}) in $LSCF_{113}$ and LSC_{214} (a) $La_{0.625}Sr_{0.375}Fe_{0.75}Co_{0.25}O_3$ (b) $La_{0.5}Sr_{0.5}Fe_{0.75}Co_{0.25}O_3$ (with an additional Sr in the simulated 2×2×2 supercells), (c) $(La_{0.5}Sr_{0.5})_2CoO_4$, and (d) $(La_{0.4375}Sr_{0.5625})_2CoO_4$. Elements are represented as: La (green), Sr (light blue), Fe (brown, center of the octahedra), and Co^{3+} (dark blue, center of the octahedra). O ions are located at the corners of all the octahedral.

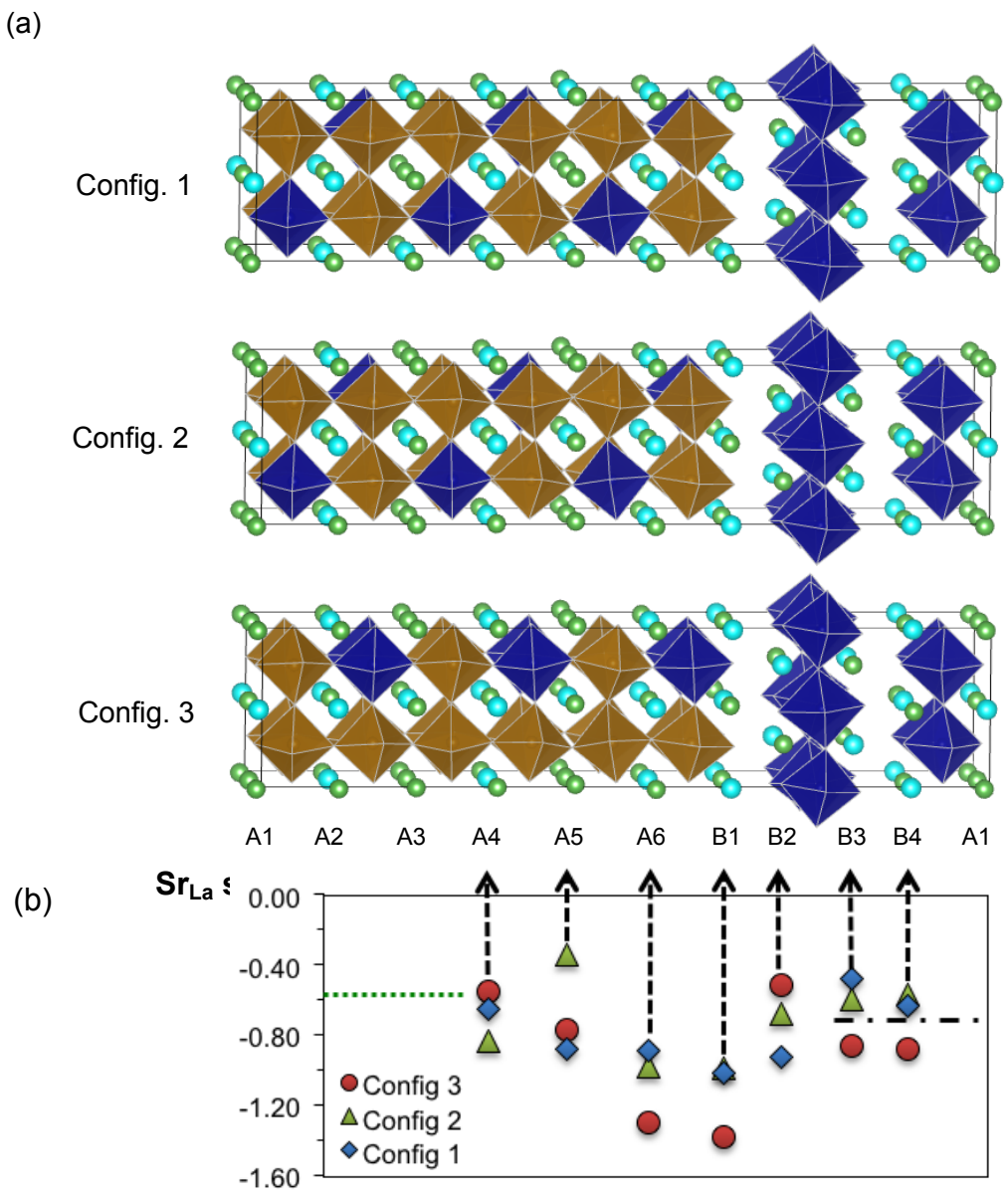

Fig. S9. (a) Schematics of the heterostructured interfaces with various A-site and B-site arrangements in the DFT simulations. $La_{0.625}Sr_{0.375}Fe_{0.75}Co_{0.25}O_3$ represents the $LSCF_{113}$ phase and $(La_{0.5}Sr_{0.5})_2CoO_4$ represents the LSC_{214} phase. Elements are represented as: La (green), Sr (light blue), Fe (brown, center of the octahedra), and Co^{3+} (dark blue, center of the octahedra). O ions are located at the corners of all the octahedra. The AO planes are numbered from A1 through A6 in the $LSCF_{113}$ and B1 through B4 in the LSC_{214} phase. The planes A1, B1 and B2

represent an interfacial region. The relative stability of Sr_{La} substitution energy relative to $La_{0.75}Sr_{0.25}CoO_3$, or $E(Sr_{La})$-$E(Sr_{La})$ of LSC_{113}(25%Sr), with variation in the Sr_{La} defect position across the AO planes. Values are relative to a bulk LSC_{113}(25%Sr) reference (y=0). Also shown is a dotted horizontal line representing the Sr_{La} substitution energies for the bulk $LSCF_{113}$ (green dotted line, $E(Sr_{La})LSCF_{113}$ - $E(Sr_{La})LSC_{113}$(25%Sr)), and a black dash–dotted line for the bulk LSC_{214} (or $E(Sr_{La})LSC_{214}$ - $E(Sr_{La})LSC_{113}$(25%Sr)). Note that the more negative values on the y-axis correspond to the easier substitution of the Sr_{La} relative to bulk LSC_{113} (25%Sr).

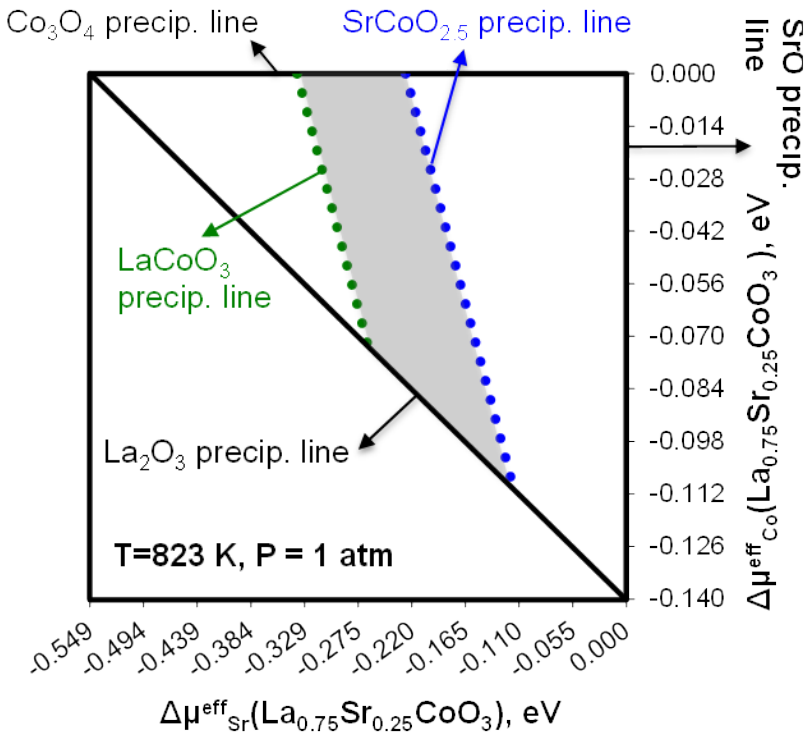

Fig. S10. Bulk $La_{0.75}Sr_{0.25}CoO_3$ phase diagram at T = 550 ºC and $p(O_2)$ = 1 atm. We note that the chemical potential of O is fixed by setting T and $p(O_2)$, while the DFT total energy of $La_{0.75}Sr_{0.25}CoO_3$ provides a constraint for the three (effective) metal chemicals so that only two (effective) metal chemical potentials are needed to construct the phase diagram. The two independent effective metal chemical potentials are represented by $\Delta\mu_{Co}^{eff}(La_{0.75}Sr_{0.25}CoO_3)$ and $\Delta\mu_{Sr}^{eff}(La_{0.75}Sr_{0.25}CoO_3)$, where $\Delta\mu_{Co}^{eff}(La_{0.75}Sr_{0.25}CoO_3)=\mu_{Co}^{eff}(La_{0.75}Sr_{0.25}CoO_3)-\mu_{Co}^{eff}(Co_3O_4)$ and $\Delta\mu_{Sr}^{eff}(La_{0.75}Sr_{0.25}CoO_3)=\mu_{Sr}^{eff}(La_{0.75}Sr_{0.25}CoO_3)-\mu_{Sr}^{eff}(SrO)$. The shaded area in the phase diagram represents the stable region for bulk $La_{0.75}Sr_{0.25}CoO_3$ vs. the $LaCoO_3$, $SrCoO_{2.5}$, Co_3O_4, SrO, and La_2O_3 oxides, based on the inequality equations - Equations (22)~(26) using the effective chemical potentials of metals of $La_{0.75}Sr_{0.25}CoO_3$, $LaCoO_3$, $SrCoO_{2.5}$, Co_3O_4, SrO, and La_2O_3.

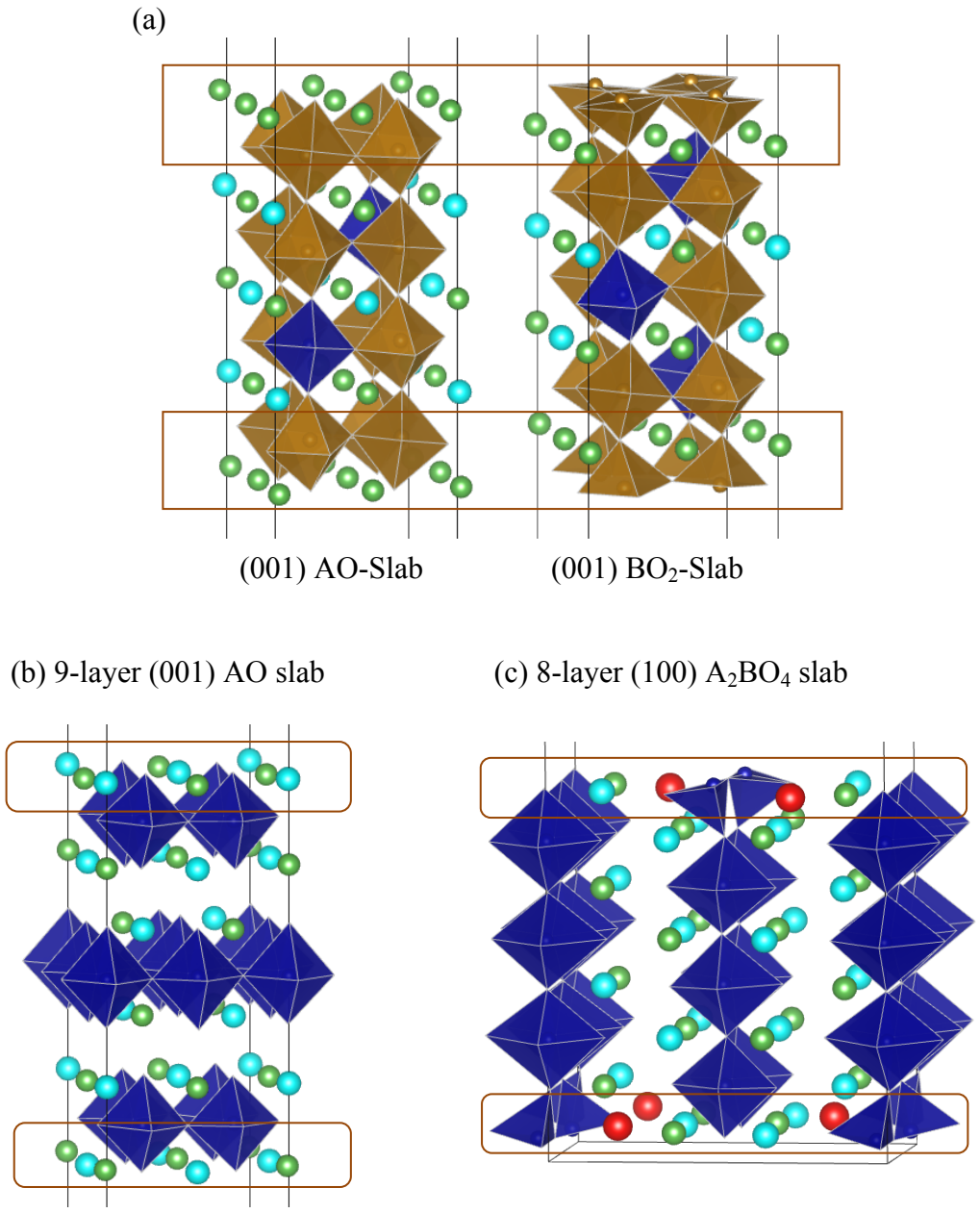

Fig. S11. (a) The LSC_{113} and $LSCF_{113}$ (001) AO (left) and BO_2 (right) slab models (b) the LSC_{214} (a) 9-layer symmetric (001) AO model and (c) 8-layer (100) A_2BO_4 slab model (all configurations shown here are after relaxation) used for the *ab initio* surface thermodynamic analysis. Green and light blue spheres represent La and Sr, while brown and deep blue polyhedral represent local Fe-O and Co-O environments, respectively. For the $LSCF_{113}$ and

LSC_{113} (001) slab models, the top (and bottom) two surface layers, where La/Sr and Co/Fe compositions ($La_{1-x}Sr_xCo_{1-y}Fe_yO_3$ with x = 0, 0.25, 0.5, 0.75, 1 y=0, 0.25, 0.5, 0.75, 1) are varied, are specified by the rectangular frames. The central part of the slabs, outside the frames, is fixed to a composition close to $La_{0.75}Sr_{0.25}CoO_3$ and $La_{0.625}Sr_{0.375}Fe_{0.75}Co_{0.25}O_3$. A total of 10 configurations (5 for the (001) AO surfaces and 5 for the (001) BO_2 surfaces) for LSC_{113}, and a total of 50 configurations (25 for the (001) AO surfaces and 25 for the (001) BO_2 surfaces) for $LSCF_{113}$, are calculated based on these 9-layer 2×2 symmetric slab models for the surface stability analysis. For the LSC_{214} (001) and (100) slabs, the top and bottom surface layers, where La/Sr compositions are varied, are specified by the rectangle frames. The rest (central) part of the slabs is fixed to the LSC_{214} composition. In the relaxed LSC_{214} (100) slab configurations, local surface relaxation of the (100) A_2BO_4 slab introduces rearrangement of the surface Co-O square pyrimadal configuration: a surface O (as shown in red) is displaced with an elongated Co-O bond (>2.8 Å) to form Co-O tetrahedral while the La/Sr-O bond is shortened (from ~2.5 Å to 2.2~2.4 Å). In the LSC_{214} surface stability analysis, a total of 6 configurations (3 for the (001) AO surfaces with surface layer Sr = 0.5, 0.75, and 1.0 and 3 for the (100) A_2BO_4 surfaces with the surface layer Sr = 0.5, 0.75, and 1.0) are investigated in this work.

(a)

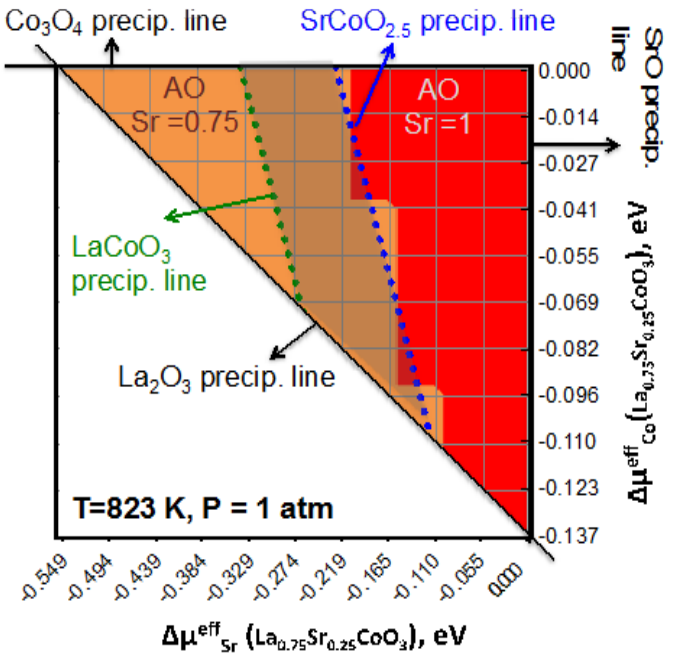
Co3O4 precip. line
SrCoO2.5 precip. line
AO
Sr =0.75
AO
Sr =1
LaCoO3
precip. line
La2O3 precip. line
T=823 K, P = 1 atm
SrO precip. line
0.000
-0.014
-0.027
-0.041
-0.055
-0.069
-0.082
-0.096
-0.110
-0.123
-0.137
-0.549
-0.494
-0.439
-0.384
-0.329
-0.274
-0.219
-0.165
-0.110
-0.055
0.000
Δμeff Co (La0.75Sr0.25CoO3), eV
Δμeff Sr (La0.75Sr0.25CoO3), eV

(b)

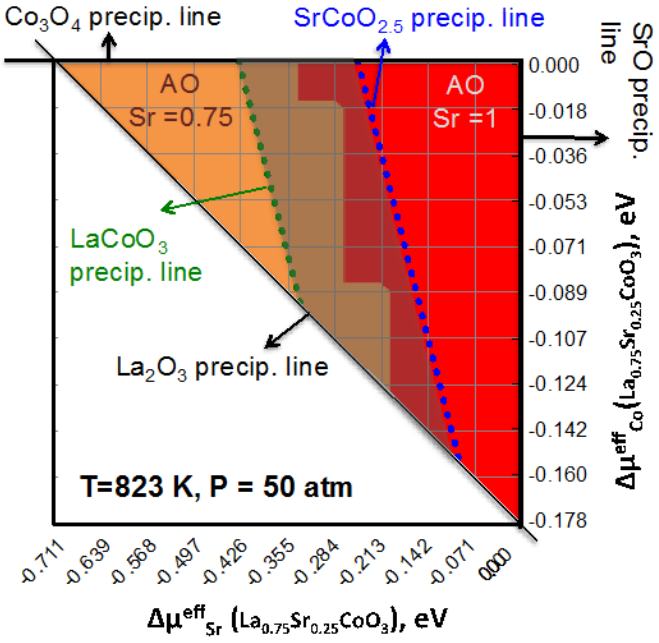
Co3O4 precip. line
SrCoO2.5 precip. line
AO
Sr =0.75
AO
Sr =1
LaCoO3
precip. line
La2O3 precip. line
T=823 K, P = 50 atm
SrO precip. line
0.000
-0.018
-0.036
-0.053
-0.071
-0.089
-0.107
-0.124
-0.142
-0.160
-0.178
-0.711
-0.639
-0.568
-0.497
-0.426
-0.355
-0.284
-0.213
-0.142
-0.071
0.000
Δμeff Co (La0.75Sr0.25CoO3), eV
Δμeff Sr (La0.75Sr0.25CoO3), eV

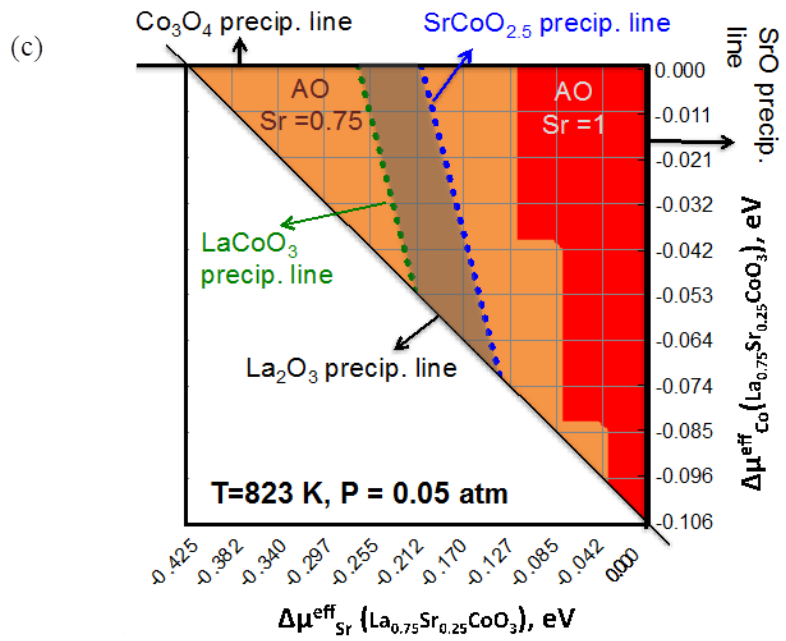

Fig. S12. The predicted $La_{0.75}Sr_{0.25}CoO_3$ surface stability diagram at T = 550 ºC (a) $p(O_2)$ = 1 atm, (b) $p(O_2)$ = 50 atm, and (c) $p(O_2)$ = 0.05 atm based on the chemical potentials of bulk $La_{0.75}Sr_{0.25}CoO_3$. The grid points represent the sampled bulk effective chemical potentials of Sr (x-axis; x=0 represents the equilibrium between $La_{0.75}Sr_{0.25}CoO_3$ and SrO) and Co (y-axis; y=0 represents the equilibrium between $La_{0.75}Sr_{0.25}CoO_3$ and Co_3O_4) in $La_{0.75}Sr_{0.25}CoO_3$, and the contour plot beyond the grid is constructed based on the calculated lowest surface energy among the investigated $La_{0.75}Sr_{0.25}CoO_3$ (001) surface configurations. The surface energy results of Fig. S12a† are provided in Table S2†.

(a) $\Delta\mu^{eff}_{Fe}(La_{0.625}Sr_{0.375}Fe_{0.75}Co_{0.25}O_3) = -0.00$ eV vs. $\mu^{eff}_{Fe}(Fe_2O_3)$

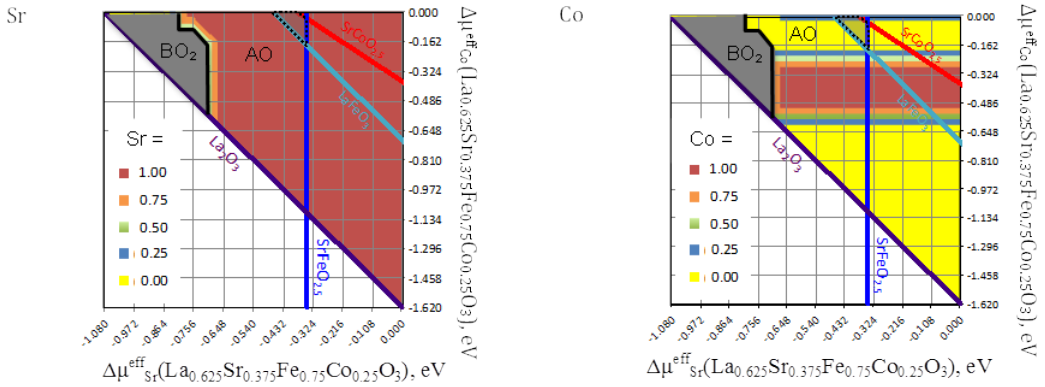

(b) $\Delta\mu^{eff}_{Fe}(La_{0.625}Sr_{0.375}Fe_{0.75}Co_{0.25}O_3) = -0.12$ eV vs. $\mu^{eff}_{Fe}(Fe_2O_3)$

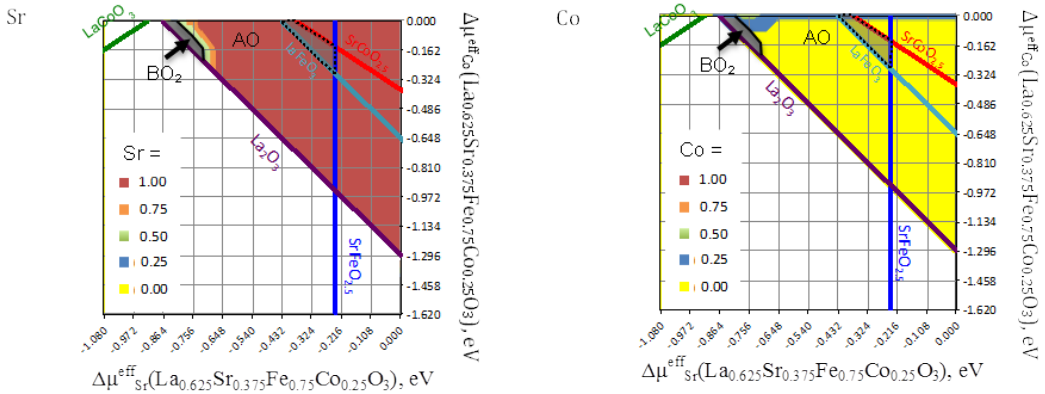

(c) $\Delta\mu^{eff}_{Fe}(La_{0.625}Sr_{0.375}Fe_{0.75}Co_{0.25}O_3) = -0.24$ eV vs. $\mu^{eff}_{Fe}(Fe_2O_3)$

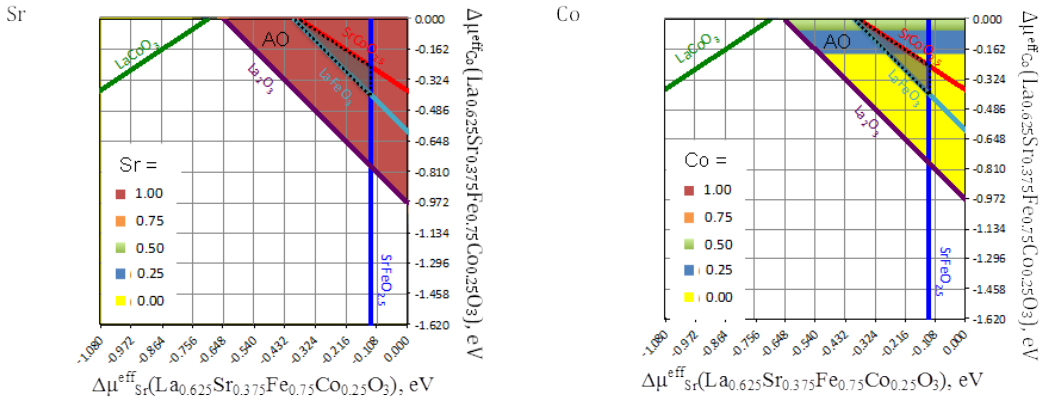

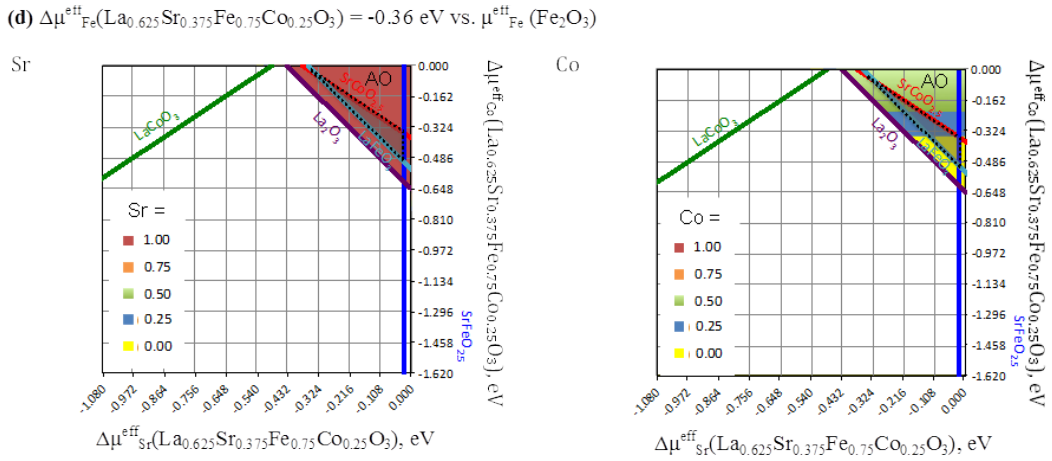

Fig. S13. The predicted $La_{0.625}Sr_{0.375}Fe_{0.75}Co_{0.25}O_3$ surface stability diagram at T = 550 ºC and $p(O_2)$ = 1 atm based on the effective chemical potentials of metal constituents in bulk $La_{0.625}Sr_{0.375}Fe_{0.75}Co_{0.25}O_3$: (a) $\Delta\mu^{eff}_{Fe}(La_{0.625}Sr_{0.375}Fe_{0.75}Co_{0.25}O_3)$ = -0.00 eV vs. μ^{eff}_{Fe} (Fe_2O_3), (b) $\Delta\mu^{eff}_{Fe}(La_{0.625}Sr_{0.375}Fe_{0.75}Co_{0.25}O_3)$ = -0.12 eV vs. μ^{eff}_{Fe} (Fe_2O_3), (c) $\Delta\mu^{eff}_{Fe}(La_{0.625}Sr_{0.375}Fe_{0.75}Co_{0.25}O_3)$ = -0.24 eV vs. μ^{eff}_{Fe} (Fe_2O_3), and (d) $\Delta\mu^{eff}_{Fe}(La_{0.625}Sr_{0.375}Fe_{0.75}Co_{0.25}O_3)$ = -0.36 eV vs. μ^{eff}_{Fe} (Fe_2O_3). The two independent effective metal chemical potentials are represented by $\Delta\mu^{eff}_{Co}(La_{0.625}Sr_{0.375}Fe_{0.75}Co_{0.25}O_3)$ and $\Delta\mu^{eff}_{Sr}(La_{0.625}Sr_{0.375}Fe_{0.75}Co_{0.25}O_3)$, where $\Delta\mu^{eff}_{Co}(La_{0.625}Sr_{0.375}Fe_{0.75}Co_{0.25}O_3) = \mu^{eff}_{Co}(La_{0.625}Sr_{0.375}Fe_{0.75}Co_{0.25}O_3) - \mu^{eff}_{Co}(Co_3O_4)$ and $\Delta\mu^{eff}_{Sr}(La_{0.625}Sr_{0.375}Fe_{0.75}Co_{0.25}O_3) = \mu^{eff}_{Sr}(La_{0.625}Sr_{0.375}Fe_{0.75}Co_{0.25}O_3) - \mu^{eff}_{Sr}(SrO)$. The grid points represent the sampled bulk effective chemical potentials of Sr (x-axis; x=0 represents the equilibrium between $La_{0.625}Sr_{0.375}Fe_{0.75}Co_{0.25}O_3$ and SrO) and Co (y-axis; y=0 represents the equilibrium between $La_{0.625}Sr_{0.375}Fe_{0.75}Co_{0.25}O_3$ and Co_3O_4) in $La_{0.625}Sr_{0.375}Fe_{0.75}Co_{0.25}O_3$, and the contour plots beyond the grid are constructed based on the calculated lowest surface energy among the investigated 50 $La_{0.625}Sr_{0.375}Fe_{0.75}Co_{0.25}O_3$ (001) surface configurations. The left-hand-side plots

in Fig. S13a†~S13d†) represent the stable (001) AO surface A-site Sr content, while the right–hand-side plots represent the stable (001) AO surface sub surface layer B-site Co content. The effective chemical potential conditions in which the BO_2 surface is more stable than the AO are presented by the grey area, which only occurs in Fig. S13a† and S13b†. The shaded area within dotted lines in each plot represents the $La_{0.625}Sr_{0.375}Fe_{0.75}Co_{0.25}O_3$ bulk stable region relative to the lower order oxides, where the boundary lines represent the equilibrium between the bulk $La_{0.625}Sr_{0.375}Fe_{0.75}Co_{0.25}O_3$ and the chosen lower order oxides ($LaFeO_3$–light blue, $SrFeO_{2.5}$–deep blue, $LaCoO_3$–green, $SrCoO_{2.5}$–red, La_2O_3–purple, SrO–x=0, and Co_3O_4–y=0). The $La_{0.625}Sr_{0.375}Fe_{0.75}Co_{0.25}O_3$ (001) surface stability analysis results suggest the most stable surfaces are the AO surfaces with the surface layer A-site Sr concentration equal to 1.00 within the bulk stable region relative to the lower order oxides.

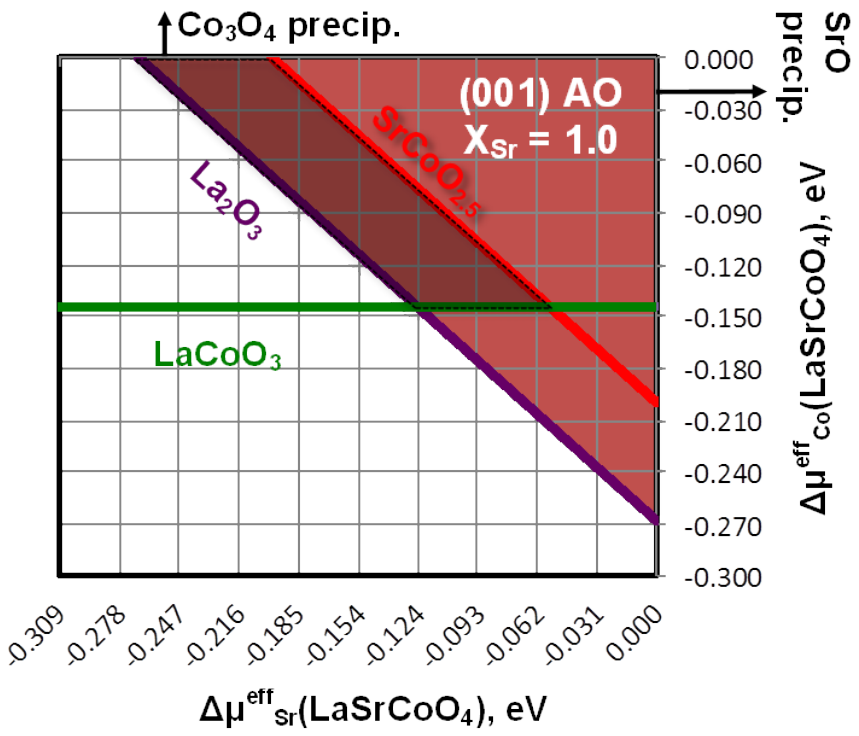

Fig. S14. Predicted contour plots for the LSC_{214} stable (001) and (100) surface layer compositions within the bulk $LaSrCoO_4$ stability boundaries (in equilibrium with La_2O_3, SrO, Co_3O_4, $LaCoO_3$, and $SrCoO_{2.5}$) based on the most stable surface energy of the investigated six $LaSrCoO_4$ slab configurations vs. chemical potentials of Sr (relative to SrO) and Co (relative to Co_3O_4) at (a) T= 550 ºC and $p(O_2)$ = 1.0 atm. Both the (001) AO and the (100) A_2BO_4 surfaces are predicted to be stable with fully enriched surface layer Sr at the A-sites within the same surface orientation. Comparatively, the surface energy of the fully Sr-enriched (100) A_2BO_4 surface is found to be a factor of 1.2 ~ 2 greater than the surface energy of the fully Sr-enriched (001) AO surface within the stable bulk $LaSrCoO_4$ region, suggesting the greater stability of the (001) AO surface with fully enriched Sr vs. the (100) A_2BO_4 surfaces.